

2014

A Comparative Study of Power Supply Architectures In Wireless Electric Vehicle Charging Systems

Bryan A. Esteban
University of Windsor

Follow this and additional works at: <http://scholar.uwindsor.ca/etd>

Recommended Citation

Esteban, Bryan A., "A Comparative Study of Power Supply Architectures In Wireless Electric Vehicle Charging Systems" (2014).
Electronic Theses and Dissertations. Paper 5237.

This online database contains the full-text of PhD dissertations and Masters' theses of University of Windsor students from 1954 forward. These documents are made available for personal study and research purposes only, in accordance with the Canadian Copyright Act and the Creative Commons license—CC BY-NC-ND (Attribution, Non-Commercial, No Derivative Works). Under this license, works must always be attributed to the copyright holder (original author), cannot be used for any commercial purposes, and may not be altered. Any other use would require the permission of the copyright holder. Students may inquire about withdrawing their dissertation and/or thesis from this database. For additional inquiries, please contact the repository administrator via email (scholarship@uwindsor.ca) or by telephone at 519-253-3000ext. 3208.

A Comparative Study of Power Supply Architectures In Wireless Electric Vehicle Charging Systems

by

Bryan Esteban

A Thesis

Submitted to the Faculty of Graduate Studies
through Electrical and Computer Engineering
in Partial Fulfillment of the Requirements for
the Degree of Master of Applied Science at the
University of Windsor

2014

Windsor, Ontario, Canada

© 2014 Bryan Esteban

A Comparative Study of Power Supply Architectures In Wireless Electric Vehicle Charging Systems

by

Bryan Esteban

APPROVED BY:

G. Rankin

Department of Mechanical, Automotive & Materials Engineering

P. Alexander

Department of Electrical and Computer Engineering

M. Sid-Ahmed, Co-Advisor

Department of Electrical and Computer Engineering

N. Kar, Co-Advisor

Department of Electrical and Computer Engineering

26 August 2014

Author's Declaration of Originality

I hereby certify that I am the sole author of this thesis and that no part of this thesis has been published or submitted for publication.

I certify that, to the best of my knowledge, my thesis does not infringe upon anyone's copyright nor violate any proprietary rights and that any ideas, techniques, quotations, or any other material from the work of other people included in my thesis, published or otherwise, are fully acknowledged in accordance with the standard referencing practices. Furthermore, to the extent that I have included copyrighted material that surpasses the bounds of fair dealing within the meaning of the Canada Copyright Act, I certify that I have obtained a written permission from the copyright owner(s) to include such material(s) in my thesis and have included copies of such copyright clearances to my appendix.

I declare that this is a true copy of my thesis, including any final revisions, as approved by my thesis committee and the Graduate Studies office, and that this thesis has not been submitted for a higher degree to any other University or Institution.

Abstract

Wireless inductive power transfer is a transformational and disruptive technology that enables the reliable and efficient transfer of electrical power over large air gaps for a host of unique applications. One such application that is now gaining much momentum worldwide is the wireless charging of electric vehicles (EVs). This thesis examines two of the primary power supply topologies being predominantly used for EV charging, namely the SLC and the LCL resonant full bridge inverter topologies. The study of both of these topologies is presented in the context of designing a 3 kW, primary side controlled, wireless EV charger with nominal operating parameters of 30 kHz centre frequency and range of coupling in the neighborhood of .18-.26. A comparison of both topologies is made in terms of their complexity, cost, efficiency, and power quality. The aim of the study is to determine which topology is better for wireless EV charging.

Contents

Author’s Declaration of Originality	iii
Abstract	iv
List of Figures	vii
List of Tables	ix
1 Introduction	1
1.1 Rationale for Adoption of Wireless EV Charging	2
1.2 Wireless EV Charging Activities Around the World	4
1.2.1 Auckland University (AU)	4
1.2.2 Korean Advance Institute of Science and Technology (KAIST)	5
1.2.3 Utah State University Power Electronics Lab (UPEL)	6
1.2.4 Oak Ridge National Laboratories (ORNL)	7
1.2.5 Massachusetts Institute of Technology (MIT)	8
1.3 An Industry Standard for Wireless Charging: SAEJ2954	9
1.4 Thesis Overview	10
2 Theory of Inductive Power Transfer	12
2.1 Overall System Perspective	12
2.2 Fundamental Laws of Operation	13
2.2.1 Ampere’s and Faraday’s Laws	13
2.2.2 Magnetic Coupling and Mutual Inductance	15
2.2.3 Resonance	17
2.3 Electrical Model of Loosely Coupled IPT Systems	20
2.3.1 Mutual Inductance Circuit Model	21
2.3.2 Mathematical Model of IPT System With Parallel Resonant Secondary	22
3 Magnetic Pad Design	27
3.1 Archimedean Spiral Coils	27
3.2 Coil Fabrication	29
3.3 Experimental Characterization of Coil Attributes	30
4 Primary Side Power Supply Design	34

4.1	EV Charging Power Supply Topologies	34
4.1.1	Series Resonant (SLC) Topology	38
4.1.2	Hybrid Series-Parallel Resonant (LCL) Topology	40
4.1.3	HF Isolation Transformer Design	42
4.2	Determination of Component Ratings	45
4.3	Switching Network Gate Driver Design	46
4.4	Physical Implementation	51
5	Comparison of Power Supply Topologies	54
5.1	Complexity and Cost	54
5.2	Efficiency	55
5.3	Power Quality	56
6	Conclusion	57
	Appendix A Derivations	58
A.1	Axially Aligned Coils	58
A.2	Axially Misaligned Coils	60
	Bibliography	63
	VITA AUCTORIS	69

List of Figures

1.1	Qualcomm Halo Wireless EV and Conductix-Wamplfer Wireless E-Bus	4
1.2	KAIST Roadway IPT Track and OLEV Bus	5
1.3	WAVE USU and U of U Wireless E-Buses	6
1.4	ORNL Stationary and Dynamic Wireless Charging Projects	7
1.5	MIT 2m Wireless Power Transfer and WiTricity Wireless EV Charger	8
2.1	IPT System Blocks	12
2.2	Ampere's and Faraday's Laws	13
2.3	Magnetically Coupled Archimedean Coils	15
2.4	Plot of equation 2.4	16
2.5	Standard RLC Network Topologies	18
2.6	Partial Series Compensation	19
2.7	Mutual Inductance Circuit Model (M-model)	21
2.8	M-model of Uncompensated IPT System with Resistive Load	21
2.9	M-model of Resonant IPT and its Equivalent When the Secondary is Referred to the Primary	23
3.1	Planar Archimedean Coils	27
3.2	Cativa V5 Mechanical Drawing of Magnetic Pads	29
3.3	Constructed Magnetic Pads	29
3.4	Experimental Test Bench for Measurement of Pad Attributes	31
3.5	Measured Pad Attributes	33
4.1	Switching Network and its Equivalent	34
4.2	Phase-Shift Control Waveforms	35
4.3	Magnetic Characteristics for Power Supply Design	38
4.4	Series LC (SLC) Topology	38
4.5	SLC FB Switching Frequency for Sustained ZVS Operation	40
4.6	Series-Parallel (LCL) Topology	40
4.7	HF Isolation Transformer Equivalent Circuit Model	42
4.8	Experimental Measurement of L_{Teq}	43
4.9	Gapped Transformer Core	45
4.10	Bootstrap Half-Bridge Gate Driver	47
4.11	Gate-Source Voltage Vs. Gate Charge	48

4.12	Gate Current and Gate-to-Source Voltage Waveforms	49
4.13	Full-Bridge Gate Driver Board	51
4.14	Schematic of Completed System Implementation	51
4.15	Full System Implementation at Rated Power	52
4.16	Primary Power Supply Implementations	52
4.17	System Operating Waveforms at Rated Conditions	53
5.1	Measured Power Supply Attributes	56
A.1	Analytical Derivation of the Mutual Inductance Using the Magnetic Vector Potential	58
A.2	Analytical Derivation of the Mutual Inductance Using the Magnetic Vector Potential	60

List of Tables

1.1	SAEJ2954 Light Duty Vehicle WPT Charging Classes	10
1.2	Summary of Primary Power Supply Topologies & Users	10
2.1	RLC Network Attributes	20
3.1	Nominal Magnetic Pad Attributes	31
4.1	Nominal Design Specifications	37
4.2	LCL Network Values	42
4.3	Measured HF Transformer Attributes	44
4.4	LCL and SLC Voltages and Currents	45
4.5	Nominal Design Specifications	46
4.6	Gate Driver Network Values and Ratings	50
5.1	Summary of Complexity and Cost Performance	55
6.1	Summary of Comparative Study	57

Chapter 1

Introduction

The drive to use electrical power in novel ways has shaped almost every aspect of technological advancement over the last two hundred years, making possible some of the most impressive achievements of our time. This now ubiquitous part of modern society has until now primarily relied on the transport of charge carriers across distance through copper conductors. Wireless inductive power transfer (IPT) - also known more generally as wireless power transfer (WPT) - is an emerging technology that uses time varying magnetic fields to safely and reliably transfer power over large air gaps to energize or charge one or more electrical loads with high efficiency. This novel technology has been quietly maturing in research labs over the past two decades and is now poised to redefine the way electrical power is consumed by society at large.

To date, IPT has been successfully adopted in clean rooms and industrial manufacturing floors for powering automated guided vehicles (AGVs) that are constrained to travel over a track and can require multi-kilowatt levels of power to operate [1, 2, 3, 4]. It has also been used to transfer small amounts of power over small air gaps for charging of portable consumer electronics such as cell phones, tablets, and electric tooth brushes [5, 6, 7, 8].

More recently though, the application of this technology for static and in-motion charging of electrified transportation such as electric vehicles, buses, and train systems over larger air gaps and misalignment has seen an explosion in research and development in academia and private industry. With an interoperability industry standard (SAEJ2954) well in progress towards completion by 2015, wireless charging of EVs has gone from being merely an obscure and exotic technology to a tangible and appealing reality.

This thesis focuses on the primary power supply topologies presently being predominantly used in wireless electric vehicle (EV) charging. In the sections to follow a brief outline of the rationale for adopting wireless over conductive charging will be presented, followed by an overview of some of the current research, development, and commercialization activities being carried out world wide in the field of wireless EV charging. The final section in this chapter will outline the objective of this thesis and present a brief overview of the work completed by the author.

1.1 Rationale for Adoption of Wireless EV Charging

Despite many potential benefits, to date, the mass adoption of electrified transportation has been greatly hindered by two key factors: 1) the perceived limitations and high cost of electric vehicles (EVs) in the mind of the average driver, and 2) the low profitability margin imposed on auto makers by the high production cost associated with current EV technology.

Concerning the first limiting factor, the term “range anxiety” was coined to describe the reluctance that many drivers have when they contemplate the possibility of changing from an internal combustion engine (ICE) vehicle to an EV. Many of these potential EV owners feel that current EV technology would limit them and radically alter their driving habits by virtue of not having the ability to drive as far on a single charge as they could on a single gas tank. Further complicating matters in the minds of potential consumers is the cumbersome EV charging process itself, which requires lengthy charging times and the handling of heavy, dirty, and possibly frozen cables. For example according to the U.S. Department of Energy, most EVs can only go about 100-200 miles before recharging, while gasoline vehicles can go over 300 miles before refueling. Also, while filling up at a gas station takes mere minutes, fully recharging the battery pack of an EV can take 4-8 hours. Even a “fast charge” to 80% capacity can take 30 min [9].

On the other hand, the size and weight of the average EV battery pack along with its associated manufacturing cost make the production of EVs less profitable to vehicle makers (because of low demand) and by extension more costly to consumers. For example, the specific weight of lithium-ion (Li-ion) battery technology is reported to be in the range of 60-96 Wh/kg, which means that the total weight of a battery pack for a vehicle requiring 20 kWh would exceed 200 kg. In addition to high weight and size, the estimated cost of Li-ion technology is about US\$700/kWh, which makes the price of an EV almost double that of its fossil fuel counterpart, with nearly half of the total cost being taken up by the battery [10, 11]. Allan Mulally, CEO of Ford Motors, confirmed the foregoing figures at the 2013 Fortune magazine’s Brainstorm Green conference in California; accordingly, Mulally indicated that the manufacturing cost of a 23 kWh battery pack for the Ford Focus EV could range anywhere between US\$12,000-US\$15,000 per car, and weighs 272-316 kg’s. Moreover, while the starting price of the ICE based Focus is around US\$22,000, the starting price of the EV counterpart is around US\$39,200 [12, 13]

In light of the aforesaid limitations, much research and development is being undertaken so as to extend the driving range of EVs and lower their cost. To this end, there are ongoing R&D efforts to improve the battery chemistry itself so as to increase its energy and power densities while also lowering its cost. On the other hand, there are a growing number of academic, private, and governmental institutions that are focusing their attention on a more promising alternative means to achieve the previously stated goals sooner, namely wireless EV charging.

The application of IPT for wireless EV charging and/or even powering is by no means new, the first practical effort to investigate this possibility was placed forth in the late 1970’s by UC Berkeley’s Partner for Advanced Transit and Highways (PATH) research team. The final product of the PATH project was a system capable of transferring 60 kW to a bus over a 7.6 cm air gap. Due to the limited semiconductor technology available at the time the system’s switching frequency was very

low (i.e. 400 Hz) resulting in large system size, high cost, and poor efficiency (i.e. 60%) [14]. With the advancements in power semiconductor technology and high speed microprocessors that have ensued since PATH, many research groups have picked up where the PATH team left off and in the last decade have been able to show that IPT technology is now ready to redefine the way EVs are charged, and more broadly to transform the way electric power is consumed by society at large.

The advantages of this novel technology are many, the following are just a few that highlight how wireless EV charging addresses the limitations presented at the outset:

Range Extension: Because it can be fully automated and scheduled, and requires no external physical intervention from a driver, wireless charging can be carried out more frequently and seamlessly throughout the normal driving cycle of an EV, thereby extending the range of the battery. If the infrastructure were in place, wireless charging could be carried out opportunistically at parking spots in urban centers or homes, at stop signs and traffic lights, as well as in areas where heavy traffic allows vehicles to slow down significantly or even come to a complete stop. Looking ahead to the future, it is conceivable to have dedicated roadway systems or lanes that allow EVs to wirelessly charge while traveling at full speed [15].

Cost Reduction: The ability to charge more frequently can result in a decreased battery size and by extension cost. For example, it has been reported that wireless charging of electric buses at scheduled stops can result in an 80% reduction of the required battery size [10]. This result can be readily extended to EVs provided that the required infrastructure is in place to support frequent in-route charging. The increased charging frequency also lowers cost in that it can extend the life of the battery by reducing the depth of discharge and by extension the wear on the battery chemistry when a full charge is carried out.

Convenience: The need to handle bulky, heavy, as well as possibly dirty, wet, and/or cold cables and plugs is eliminated, as is the need to brave the elements in order to plug-in. This is particularly convenient and practical in wintery climates where a sudden rise and drop in temperature can result in a plug that is fused by ice into the charging receptacle. Additionally, because the charging process can be made fully autonomous on demand, a charging schedule that fits a user's average driving cycle or a desired charging pattern throughout the day can be programmed resulting in a greatly enhanced user experience [15].

Safety: Careful design of the magnetic couplers that facilitate the wireless transfer of energy along with field shaping techniques mean that users will be shielded from exposure to field emissions that are above established regulatory levels, thus ensuring their safety. Increased safety is also achieved by the removal of the potential trip hazard presented by a charging conductor in areas of heavy foot traffic. Additionally, because the system is largely out of sight and reach due to its being either embedded in the road or integrated on the vehicle, the risk of electrocution that is present with accidentally damaged charging cables is minimized, as is the risk of vandal tampering and theft [16, 17, 18].

Aesthetics: The removal of cords can result in significant reduction to the system's footprint, thereby enhancing the visual appeal of a street, or other public or personal space where a wireless charger might be installed.

The section to follow will present an overview of wireless EV charging endeavors around the globe.

1.2 Wireless EV Charging Activities Around the World

Significant advancements in the development of wireless power technology have been made over the last decade. What follows is of necessity a limited and brief summary of some of the most relevant research activities in the area of wireless EV charging.

1.2.1 Auckland University (AU)



Figure 1.1: Qualcomm Halo Wireless EV and Conductix-Wamplfer Wireless E-Bus

Professors Grant Covic and John Boys of the department of electrical engineering at Auckland University (AU) are the modern pioneers of wireless power technology (the first pioneer in the truest sense was Nikola Tesla [19]).

The earliest work on wireless power undertaken at AU extends as far back as 1989 and focused on the application of inductive power transfer for automated guided vehicles (AGVs) which are used in industrial manufacturing facilities and clean rooms and have reasonably good magnetic coupling because of being constrained to traveling on a track system [2, 20, 21]. Development of these early systems set the theoretical and technical framework for the more challenging R&D involved with wireless EV charging where greater positional freedom is required. Much of the current theoretical knowledge base underlying modern IPT technology can be credited to the work of Professors Covic and Boys.

The application of the standard mutual inductance circuit model (M-model) to the study of loosely coupled, resonant, wireless power transfer systems has been largely championed by AU along with the use of magnetic simulation software packages for characterization and optimization of the complex magnetic behavior of the coupled coils involved in IPT system [22, 16, 17, 23, 24, 25].

In the area of EV charging, AU has produced a number of published works and patents on the optimization of novel magnetic pad geometries that result in enhanced magnetic coupling while

allowing greater positional freedom and reduced size and cost [17, 26, 27, 18, 28]. Much work has also been completed on the development of low cost, constant current source, primary power supplies that can tolerate the unique operating conditions imposed by wireless EV charging. The LCL-T power supply architecture with fix-frequency operation, a low energy DC bus, high frequency (HF) bridge isolation transformer with integrated inductance, and phase-shift control of the inverter legs is one major contribution in this area, with many commercialization effort currently using the topology for field testing of wireless EV charging.

Another important contribution by AU, perhaps the most important one, is the identification and full characterization of system instability issues (bifurcations) that arise for certain extreme loading conditions [29, 30]. AU also proposed a novel way of addressing the issue, known as secondary side decoupling control, whereby a power electronics regulator is used on the receiver side to modify the reflected loading seen at the primary so that the system's overall loading profile is always maintained in a stable operating region [1].

Finally, in recent years, AU has developed multiphase/multi-kilowatt track systems for dynamic wireless charging of Roadway Powered Electric Vehicles (RPEVs) [31].

AU is also playing a significant role in the commercialization of wireless power technology with its involvement in the SAEJ2954 Wireless EV Charging standards committee and the licensing of its intellectual property to: materials handling giant Daifuku (Japan), EV wireless charging developer Qualcomm Halo (USA/New Zealand), and wireless powered materials handling systems and wireless e-bus maker Conductix-Wampfler (Germany) to name a few.

1.2.2 Korean Advance Institute of Science and Technology (KAIST)



Figure 1.2: KAIST Roadway IPT Track and OLEV Bus

Another major academic contributor to the progression of wireless charging is the Korea Advanced Institute of Science and Technology (KAIST). KAIST researchers led by Professor Chum T. Rim have rapidly developed and deployed a series of RPEV's that have come to be known as On-line Electric Vehicles (OLEVs). Each system uses long segmented primary power rails embedded in the roadway to couple power to one or more traveling EVs.

Since 2009 a total of five different types of OLEV systems have been developed, with each new generation showing marked improvements in power level, efficiency, tolerance to large air gaps and misalignment, as well as reduction in system size and cost.

The first generation (G1) was a 3 kW concept demonstration EV, followed by a second (G2) 6 kW proof of concept for buses. The third generation (G3) included a 15 kW OLEV passenger car as well as several train and bus systems with the same power rating. The G3 train systems have been in operation at the Seoul Grand Park, Korea, since 2010, and the bus systems have been successfully deployed at Yeosu EXPO (2012) and even more recently at a 48 km long commercial route in Gumi, Korea. The fourth and fifth generations of OLEV are still under development for possible future deployment and will have a 25 kW power rating [32, 33].

KAIST holds patents on novel IPT coil designs that constructively shape the flow of the main magnetic field while actively canceling the remaining stray fields that are associated with very loosely coupled magnetic systems [34]. Mechanically durable primary power supply rails that withstand the mechanical wear imposed on roadways have also been proposed at KAIST. Novel work has also been undertaken on the development of robust, yet simple, primary power supply architectures. In contrast with AU, KAIST has adopted the series resonant power supply scheme, along with control techniques that result in constant current source operation for almost all practical operating conditions [33, 35, 10].

Also in contrast with AU, KAIST has advanced the theoretical state of the art by adopting the alternate transformer circuit model (T-model) in their characterization of wireless power transfer systems. More recently, an improved magnetic mirror model (IM³) for finite width, infinite permeability, mono and dual coils was developed and used to obtain closed form solutions of the magnetic flux density of coils used by KAIST in their OLEVs [36].

The aggressive pace of advancement evident in the many practical OLEV systems developed and deployed in span of merely six years has been largely supported and propelled by the Korean government, with some US\$50 million in funding provided in support of KAIST's endeavors [32].

Finally, and not surprisingly, KAIST is also an active participant in the SAEJ2954 Wireless EV charging standards committee.

1.2.3 Utah State University Power Electronics Lab (UPEL)



Figure 1.3: WAVE USU and U of U Wireless E-Buses

Formerly known as Energy Dynamics Lab (EDL), UPEL has been involved in the development and commercialization of large scale IPT systems for on-route charging of electric buses in North America since 2010. It has contributed to the state of the art by publishing works on LCL-T power supplies as well as on a novel dual side control scheme that ensures a sustained end-to-end system efficiency above 90% over a 200% change in coupling [37, 38].

As part of its commercialization efforts, UPEL's spin-off company, Wireless Advanced Vehicle Electrification (WAVE), has successfully deployed the first wireless powered bus systems in North America. The first system is a 25 kW wireless E-Bus that charges autonomously at several stops throughout its route on the Utah State University Campus in Logan, Utah. A 50 kW system was also deployed at the University of Utah campus in downtown Salt Lake City, Utah in early 2013. Currently WAVE is in the process of deploying similar systems in Monterrey, New Mexico; McAllen, Texas; and Lancaster and Palmdale, California. The California based systems will span a route covering 160 miles per day, making it the longest distance traveled by an E-Bus powered by wireless charging technology.

1.2.4 Oak Ridge National Laboratories (ORNL)



Figure 1.4: ORNL Stationary and Dynamic Wireless Charging Projects

One of the most active US government labs in the field of wireless EV charging is ORNL. Under the technical direction of Dr. John Miller and Dr. Omer Onar, ORNL's Power Electronics and Electric Machinery Group has been investigating static and in-motion wireless charging since late 2010. Along the way ORNL has made contributions to the state of the art in its research of the series resonant primary power supply architecture for both static and dynamic wireless charging, demonstrating how a combination of phase-shift and DC-link voltage control along with discrete switching frequency tuning over the system's range of coupling can ensure power flow regulation while maintaining a reduced volt-ampere stress on the power supply. ORNL used the series topology in its 3.3 kW, 7 kW, 10 kW, and 20 kW systems [39, 40, 41, 42, 43].

ORNL has also developed and tested a unique wireless roadway power system that uses real-time sequenced activation and deactivation of segmented roadway coils to wirelessly charge a passing EV. The system uses a dedicated short range communications (DSRC) link to synchronize coil

activation/deactivation with the vehicle's moving position. The system was reportedly the first of its kind anywhere [44, 45].

In implementing their in-motion charging system ORNL also observed and characterized large periodic power fluctuations that occur on both the grid and vehicle side as each coil is rapidly energized and then de-energized. Moreover, ORNL also proposed and successfully implemented a scheme that significantly decreases (smooths out) the said transients by means Li-ion capacitor banks on the grid side and double layer carbon ultra capacitors on the vehicle sides.

Finally, with the aid of commercialization partner Evatran, ORNL fully retrofitted an EV with WPT technology which will be deployed on the main campus of the University of Tennessee as a mail delivery vehicle. ORNL is also heavily involved in the J2954 wireless charging initiative.

1.2.5 Massachusetts Institute of Technology (MIT)

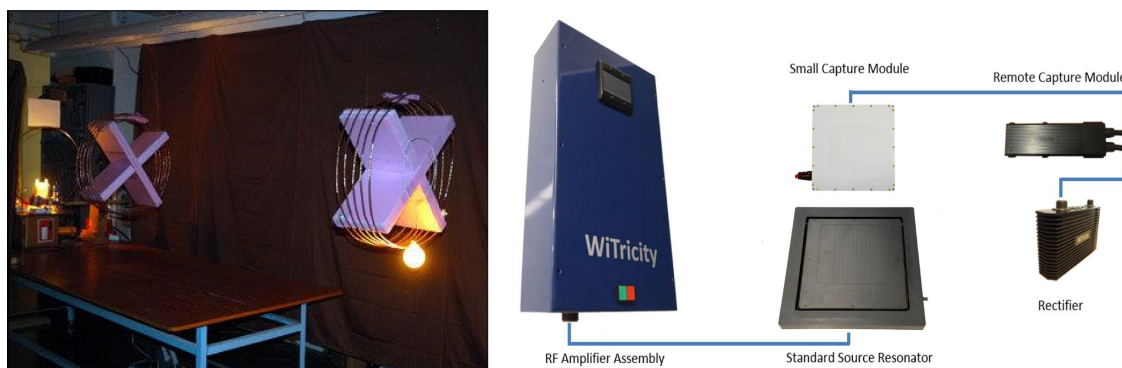


Figure 1.5: MIT 2m Wireless Power Transfer and WiTricity Wireless EV Charger

In 2007 a team of theoretical physicists at MIT captured global attention when they transferred 60 watts over a 2 meter air gap and used it to energize an incandescent light bulb. The feat was achieved using self-resonant coils operating at 9.9 Mhz. The primary side power supply used was a high power Colpitts oscillator built with a vacuum tube as its amplification element, two large air core tunable capacitors, and a single turn loop of hollow copper tubing (much like the ones used in refrigeration systems). The oscillator's inductive element was placed next to a larger multi-turn helical coil that was open circuited (i.e. its terminals were not connected to anything). Because of the high frequency used, self-resonance could be achieved by means of the helical coils distributed parasitic capacitance, resulting in a very high quality factor resonant system ($Q > 9000$). The receiver coil was identical to the source coil and also self-resonant at the operating frequency. The load was connected to a small single turn loop of wire which was placed next to the receiver resonator [46, 47].

Though the reported end-to-end efficiency of the system was only about 15% it prompted so much interest from both the public and private sphere that the spin-off company WiTricity was created in order to further develop the technology so that it could be used in practical ways. Since its registration in 2008 WiTricity has been very active in developing wireless power technologies for a host of applications including: wireless powering of TV's and household appliances; charging of

laptops, tablets, and cell phones; wireless EV charging; charging of implantable medical devices, and the development of wireless residential and commercial infrastructure.

WiTricity presently offers 3.3 kW and 7.7 kW wireless EV charging systems and is actively involved in the development of J2954. Among some of its licensing partners in the automotive sector are Toyota, Audi, BMW, and Delphi. Toyota has announced that it will make a WiTricity based WPT ready EV available to consumers in 2016.

While the specific technical details of WiTricity's primary power supply topology for EV charging applications is not formally published anywhere, a close look at its patents and on-line images of their WiT-3300 and WiCAD products would appear to indicate that it is using an LCL architecture of sorts [48].

1.3 An Industry Standard for Wireless Charging: SAEJ2954

In late 2010 the Society of Automotive Engineers (SAE) assembled an international task force, formally known as SAEJ2954, to develop a working industry standard that establishes the minimum performance and safety criteria for wireless charging of plug-in hybrid electric vehicles (PHEVs) and plug-in electric vehicles (PEVs). There are a number of topics under the overall scope of J2954, including:

1. Classification of different charging types and minimum efficiency per charging type.
2. Interoperability including center operating (resonant) frequency of charging, primary and secondary power electronic topologies, coil geometries and minimum coupling.
3. Communications and software protocols.
4. System testing and validation.
5. Parking alignment between the vehicle secondary coil and the primary coil of the wireless charging unit.
6. Location of the charger on-board the vehicle and its orientation.
7. Safety considerations including foreign object detection (both organic and inorganic); acceptable magnetic field levels; charging battery state of charge levels and rate; temperature development tests; and electric shock.
8. Design validation test and wireless charging verification test.

The J2954 task force is composed of vehicle original equipment manufacturers (OEM's), wireless charging technology developers, infrastructure suppliers, as well as academic and governmental organizations. The following is a list of the members in each of the foregoing groups:

OEM's:

Audi, BMW, Chrysler, Coda, Daimler, Fisker, Ford, GM, Honda, Mitsubishi, Nissan, Phoenix, Toyota, and Proterra.

Tier 1 Suppliers:

Delphi, Magna, Maxwell, Panasonic.

IPT Technology Developers:

Conductix Wampfler, Evatran, Qualcomm, KAIST, Momentum Dynamics, LG, SEW, WiTricity.

Infrastructure Companies:

Better Place, NRG Energy, Qualcomm.

Government Organizations:

US Department of Energy (DOE), US Department of Transportation (DOT), US Environmental Protection Agency (EPA), US Argonne National Lab (ANL), US Oak Ridge National Lab (ORNL), US Energy Dynamics Lab (EDL), US Idaho National Lab (INL); Japan Automobile Research Institute (JARI), Electric Power Research Institute (EPRI), Underwriters Laboratories (UL), and TUV North America

As of the publication date of this thesis, the J2954 task force has agreed upon the charging classes for light duty vehicles (Table 1.1), as well as on an operating frequency of 85kHz and associated frequency band in the range of (81.38 - 90.00)kHz. Among some of the key items still pending completion by the task force are the minimum magnetic coupling coefficient, positional alignment scheme, coil geometries, and minimum overall system efficiency. The tentative completion time frame for a first draft of the J2954 technical information report (TIR) is slated for sometime in 2015.

Table 1.1: SAEJ2954 Light Duty Vehicle WPT Charging Classes

Classification	WPT1	WPT2 Private/Public Parking	WPT3 Fast Charge
Max Input WPT Power	3.7 kW	7.7 kW	22 kW

1.4 Thesis Overview

Table 1.2: Summary of Primary Power Supply Topologies & Users

Organization Name	Primary Power Supply Topology
Auckland University	LCL
Korea Advanced Institute of Science & Technology	SLC
Utah State University Power Electronics Lab	LCL
Oak Ridge National Laboratory	SLC

The previous sections have readily shown that wireless EV charging is being aggressively developed for rapid commercialization and mass deployment over the next decade. The review of different research projects world wide presented in section 1.2 also highlighted the fact that two primary side power supply topologies have emerged as strong candidates for final adoption in a standardized deployment of wireless EV charging; Table 1.2 is a summary of the two topologies and their respective users/proponents. Moreover, section 1.3 showed that the industry desires a standardized primary topology. Not to be overlooked is the fact that, beyond interoperability concerns, the establishment

of a standard primary topology is of great interest to OEM's and Tier 1 suppliers who will ultimately favor a topology that in addition to complying with the minimum criteria set by J2954 also results in reduced size, complexity, and cost.

In view of the foregoing need, this thesis has as its aim to complete a theoretical and practical comparative study between the two most common primary side power supply architectures being used in wireless EV charging, namely the voltage feed full-bridge series resonant topology (SLC), and the voltage feed full-bridge hybrid series-parallel resonant topology (LCL). The comparative study will be presented in the context of designing a 3 kW, static, wireless EV charger that can operate over a range of coupling in the neighborhood of 0.18-0.26.

The chapters that follow will present the following topics: Chapter 2 will lay a brief theoretical foundation of inductive power transfer; chapter 3 will describe the practical design, fabrication, and testing of the magnetic pads that are used to couple power wirelessly; chapter 4 is the center piece of the thesis, it will detail the theoretical design of the two topologies being compared as well as their practical implementation and testing; chapter 5 will discuss and compare the measured performance of both topologies in terms of their complexity, cost, efficiency, and power quality; finally, chapter 6 will conclude with a brief review of the completed work as well as offer possible areas of future research stemming from this work.

Chapter 2

Theory of Inductive Power Transfer

2.1 Overall System Perspective

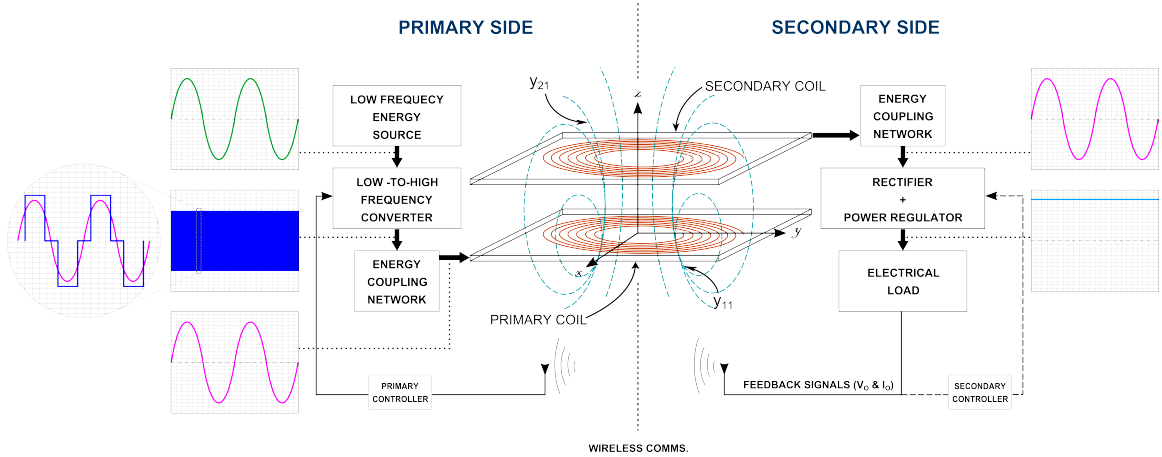


Figure 2.1: IPT System Blocks

A simplified IPT system block diagram is shown in Figure 2.1, it shows that in general, such a system is made up of two electrically isolated entities known as the primary and the secondary sides. The primary side can be further partitioned into four subsystems: a low frequency (LF) source of electrical energy, a power conversion stage that converts the LF energy to high frequency (HF), an energy coupling network (ECN) that is used to efficiently inject the HF energy to the next stage, and a magnetic field source coil also commonly referred to as a magnetic pad. In the literature, the first three blocks are commonly lumped together and referred to as the IPT power supply [20, 49].

Across a large and variable air gap, the secondary side can be similarly subdivided into an interconnection of three subsystems: a magnetic field sink coil commonly referred to as a pick-up, another ECN that serves the same purpose as the one on the primary side, and a power processing and

conditioning stage that converts the HF energy to stable DC energy which is then used to drive an electrical load. For dynamic systems where there exists a need to actively regulate the power flow due to positional changes between the source and sink coils and/or changes in loading, real-time control may be achieved by embedded control systems on either the primary or secondary sides or on both; the later control scheme is often referred to as dual-side control.

2.2 Fundamental Laws of Operation

At the heart of all modern inductive power transfer systems are two basic phenomena: electromagnetic induction and electrical resonance. The first phenomena is solidly based on two of the oldest laws of classical electromagnetics: Ampere's and Faraday's laws. The latter has also been long known and widely used in many other more common and well established applications.

The use of resonance enhanced magnetic induction to transfer power wirelessly is by no means new, it was first proposed at the turn of the century by Nikola Tesla, and many of his early experiments with Tesla coils bear this out [19]. The recent rebirth of Tesla's dream has been largely enabled by the development of semiconductor technology and the related field of power electronics. Power electronics allows for the efficient conversion of low frequency energy to high frequency energy at very high power levels and frequencies.

This chapter will present a brief summary of the key theoretical framework needed to understand modern inductive power transfer systems.

2.2.1 Ampere's and Faraday's Laws

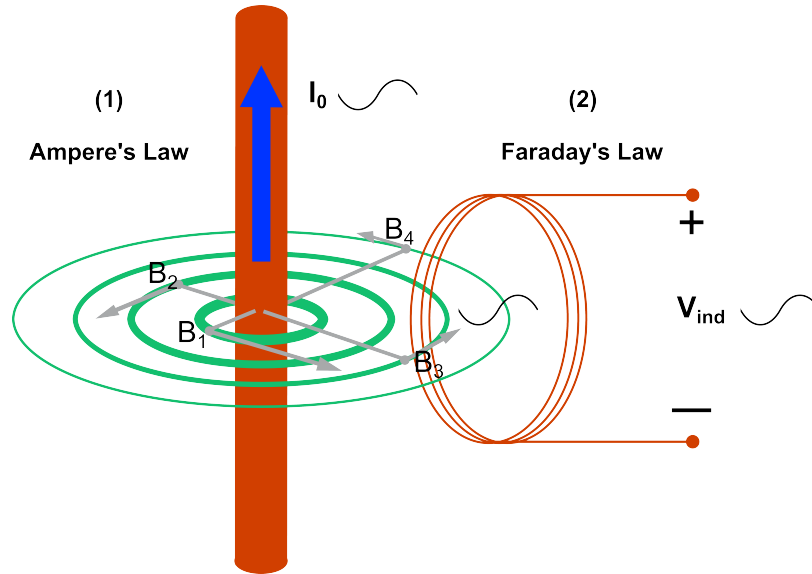


Figure 2.2: Ampere's and Faraday's Laws

$$\oint \mathbf{B} d\mathbf{l} = \mu I_0 \quad (2.1)$$

Formulated in 1824, Ampere's law (2.1) states that the current I_0 flowing in a conductor will produce a magnetic flux density field \mathbf{B} in the region surrounding that conductor as illustrated in Fig.2.2. In general, the strength or amplitude of the foregoing field at any given point in space will be directly proportional to the size of the current causing it and inversely proportional to the distance of the field point to the source current; put simply: the larger the current, the stronger the field, and the further away from the current, the weaker the field. Moreover, if the field causing current is time-varying, the resulting field will also be time-varying, having all of the same frequency components of the causal current.

The \mathbf{B} -field in Ampere's law is known in electromagnetics as a storage field because it stores a reservoir of stationary (i.e. non-radiative, non-propagating) potential energy throughout the space where it is distributed. The energy density of the foregoing field decays at a rate proportional to the inverse of the cube of the distance from the source ($\frac{1}{d^3}$), consequently, it is also often called a near field.

In inductive power transfer systems, Ampere's law is seen in operation on the primary side where a signal source is used to inject high frequency energy to an inductive structure so as to produce a magnetic field. The distance over which the produced field may be used as a power link is limited to being well within one quarter of the wavelength of the signal driving the system ($d \ll \frac{\lambda}{2\pi}$), this regime of operation is often called the quasi-static or evanescent wave regime of operation.

$$V_{ind} = -N_2 \int \frac{\partial \mathbf{B}}{\partial t} d\mathbf{a} \quad (2.2)$$

Faraday's law (2.2), formulated in 1836, says that a time-varying magnetic flux through the area enclosed by a semi-closed conducting path will induce a time varying potential difference, V_{ind} , between its two terminals. The magnitude of the induced voltage is directly proportional to the inducing field's amplitude, rate of change, and to the number of times, N , the conducting path encloses/intercepts the field. Consequently, the stronger the field, the faster it changes over time, and the more number of times the conductor wraps around the flux field, the larger the potential difference that will be induced.

If the semi-close conducting path in Faraday's law is terminated by means of an electrical load such as a resistor R , then the induced voltage will drive a current through this load, which will in turn deliver power at the rate of $P = \frac{V_{ind}^2}{R}$ watts.

In inductive power transfer systems Faraday's law is in operation on the secondary side, where a coil is used to pick up as much of the potential energy stored in the time varying \mathbf{B} -field produced by the primary as possible.

The design of the inductive structures that couple power in an IPT system relies heavily on an understanding of the spatial distribution of the \mathbf{B} -field that a given coil geometry will produce as it is directly related to the power that can be transferred. Moreover, due to established regulations, a

thorough understanding is also required so as to ensure that field exposure levels for any potential users or by-standards are within established limits. Because obtaining closed form solutions of the \mathbf{B} -field directly from Maxwell's equations for most practical coil arrangements is not possible (or in some cases possible but not practically useful), this and other related field quantities are often obtained via finite element analysis (FEA) software packages such as: Ansys Maxwell, JMAG, COMSOL, MAGNET, HFSS, and others.

2.2.2 Magnetic Coupling and Mutual Inductance

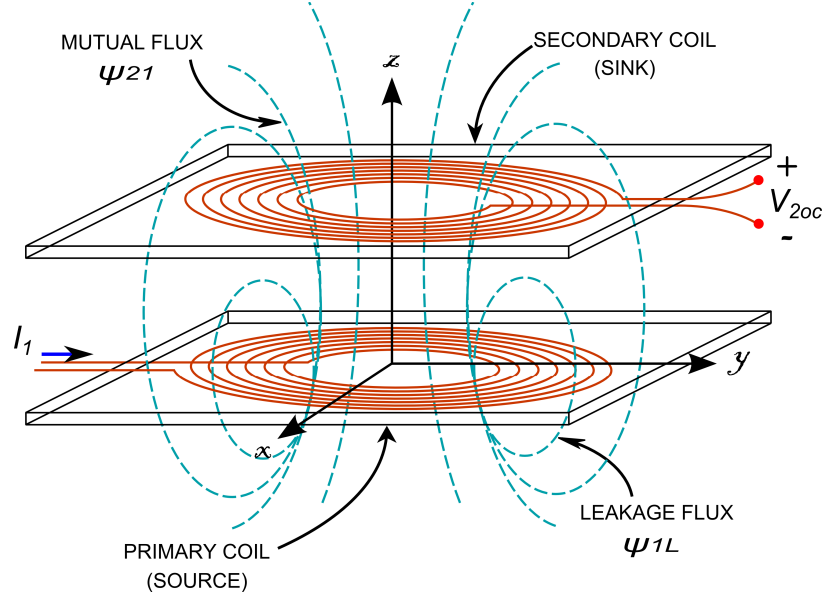


Figure 2.3: Magnetically Coupled Archimedean Coils

As implied in the last section, all IPT systems rely on the complimentary interaction of Ampere's and Faraday's laws to wirelessly transfer power via time-varying magnetic fields. The electromagnetic structures that participate in the energy exchange described by these two laws are said to be magnetically linked over an air gap through a shared magnetic field such as that illustrated by the mutual flux lines in Fig.2.3. In such a system, the ability of the primary coil to induce an open circuit voltage, V_{2oc} , in the secondary one some distance away, when energized by an alternating current, is known as the mutual inductance, M . This important property of all magnetically coupled systems is formally defined in classical electromagnetics as:

$$M_{21} = \frac{N_2 \psi_{21}}{I_1} \quad (2.3)$$

In (2.3) ψ_{21} is the magnetic flux that links the two coils, which is often only a small fraction of the total flux generated by the primary for loosely coupled coils (the coupling coefficient, k , is defined as the ratio of the mutual flux to the total primary flux); N_2 is the number of turns that make up the secondary coil and that actually intercept ψ_{21} . I_1 is the excitation current that energizes the primary coil and sets up the magnetic field. Since ψ_{21} is proportional to the number of primary

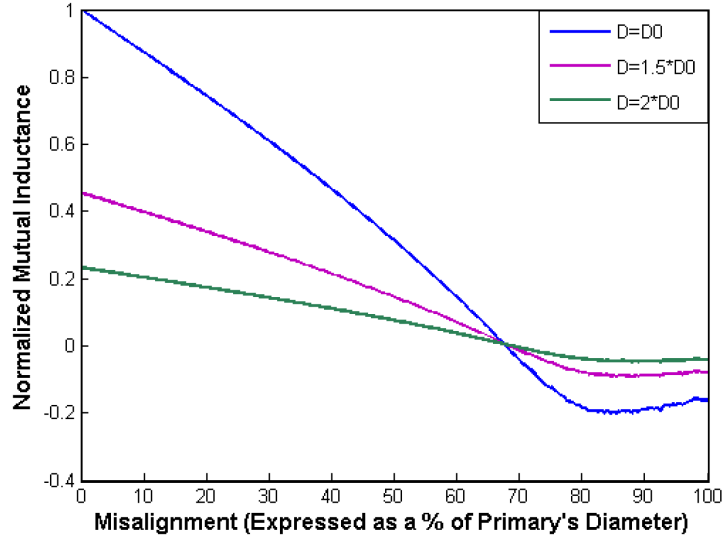


Figure 2.4: Plot of equation 2.4

turns, I_1 , medium permeability, and surface area that intercept the mutual flux, it is perceivable from (2.3) that M_{21} is predominantly a geometrical quantity, having to do with the sizes, shapes, and relative positions of the coils.

The role played by the primary and secondary coil areas, as well as by their axial alignment can be readily discerned by using the vector magnetic potential to derive M as a function of the coil-to-coil separation and axial alignment distances, z and m respectively (See Appendix A for the derivation):

$$M_{21}(z, m) = \sum_{i=1}^{N_1} \sum_{j=1}^{N_2} \frac{\mu_0 (\pi a_i^2) (B_{eff,j})}{\pi (\sqrt{b_j^2 + z^2})} \quad (2.4)$$

where B_{eff} is defined as:

$$B_{eff} = \frac{1}{180^\circ} \cos^{-1} \left(\frac{am}{a^2 + b^2} \right) \pi a^2 + \frac{1}{180^\circ} \cos^{-1} \left(\frac{bm}{a^2 + b^2} \right) \pi b^2 - \left(\frac{m}{a^2 + b^2} \right) \left[\sqrt{\frac{m^2}{(a^2 + b^2)^2 + 1}} \right] (a^3 + b^3) \quad (2.5)$$

As is evident from (2.4), both the primary and secondary areas of the coupled coils scale M . Moreover, the variable effective area of the secondary, B_{eff} , seen by the primary flux when misalignment takes place acts as a nonlinear scaling factor (Fig.2.4).

Conventional inductively coupled systems such as transformers, close proximity chargers, and induction motors are tightly coupled, having coupling coefficients in the range of 0.92-0.98. On the other hand, in the more recent loosely coupled IPT systems, coupling coefficients are typically in the range of 0.1-0.3, making such systems very loosely coupled.

The fraction of the flux that is not intercepted by the secondary, shown in Fig.2.3 as ψ_{1L} , is pro-

portional to $(1 - k)$ and is traditionally called the leakage flux. These stray fields are lost from the perspective of transferring power to the secondary. In loosely coupled systems, very large leakage fields result in large inductive reactances ($Z = j\omega L_{lkq}$) that can be modeled as being in series with the windings of the primary and secondary. These large reactances severely limit the flow of primary current that causes the mutual flux and the flow of secondary current which delivers power to the load.

2.2.3 Resonance

Resonance can occur in all physical systems where energy is transferred by waves. In the most general sense, resonance is a phenomenon whereby a dynamic system's inherent opposition to energy storage and transfer between two or more storage mechanisms is at a minimum. Such a condition results when an external excitation injects energy to the system at frequencies that closely match one or more of the system's inherent oscillatory modes, also known as natural frequencies. These inherent system modes are commonly known as resonant frequencies, and the sustained large amplitude oscillations that can result by driving a system at such frequencies, even with small excitations, is what is commonly known as resonance.

While a system operating at resonance has an enhanced ability to store and transfer energy over its time cycles of operation, there are always practical limitations that result in some energy being lost or dissipated by the system from cycle to cycle. Such energy losses are called damping and result in the gradual decrease in amplitude of a system's oscillatory time response.

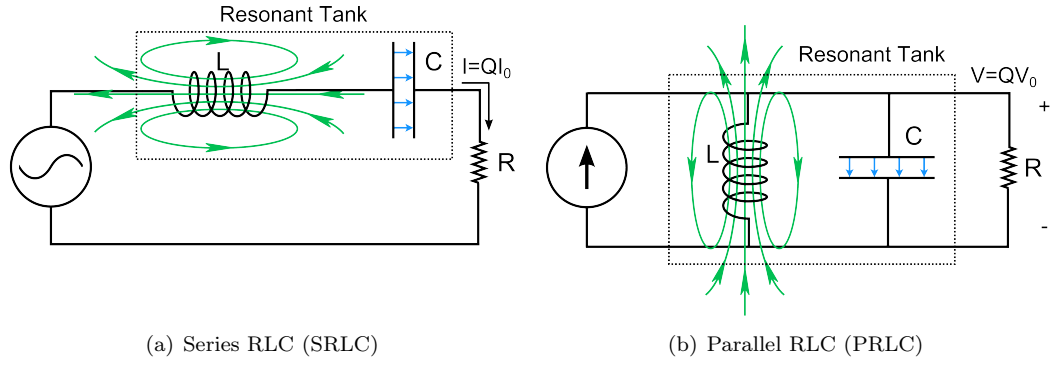
In general, the quality or Q factor of a resonant system is a dimensionless quantity that characterizes the extent to which the system is undamped and is formally defined in the context of a sinusoidally driven resonator as the ratio of the energy stored in the resonator to the energy supplied by a generator, per cycle, to keep signal amplitude constant, at the resonant frequency, f_0 , where the stored energy is constant with time. Mathematically this definition is expressed as:

$$Q = 2\pi f_0 \frac{\text{EnergyStored}}{\text{EnergyDissipated}} \quad (2.6)$$

An alternative definition of the Q factor that is relevant to the work to be presented in the sections to follow is the ratio of a system's resonant frequency to its bandwidth:

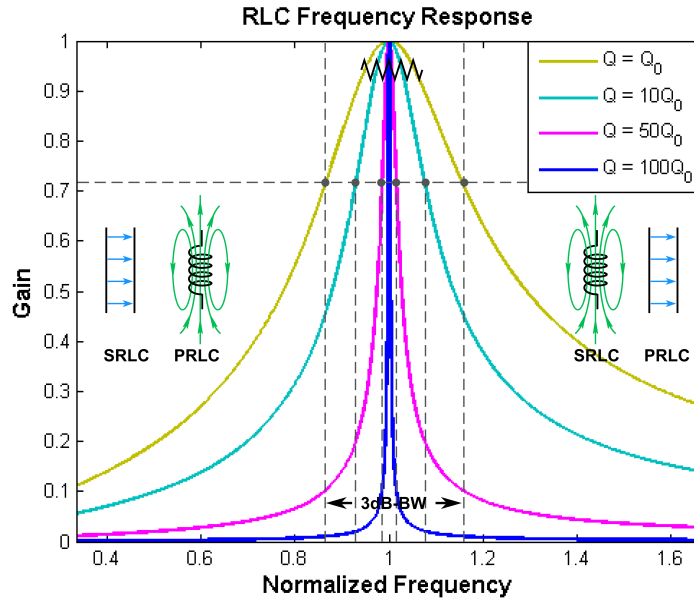
$$Q = \frac{f_0}{BW_{3dB}} \quad (2.7)$$

This alternative definition is useful in estimating the Q of a system experimentally. For example, in the case of a resonant RLC circuit (Fig.2.5), the network can be readily driven with a variable frequency signal source while observing the voltage output with an oscilloscope. The frequency at which the output has the highest amplitude is the resonant frequency. Moreover, the difference between the two frequencies on each side of f_0 where the peak signal amplitude has dropped by 30% of the maximum is what is conventionally defined as the 3db bandwidth (BW). This definition also shows that the higher the Q the narrower the system's bandwidth will be, and the more sensitive to



(a) Series RLC (SRLC)

(b) Parallel RLC (PRLC)



(c) RLC Frequency Response

Figure 2.5: Standard RLC Network Topologies

changes in tuning.

In an electrical system made up of energy storage elements such as capacitors and inductors (Fig. 2.5(a) and 2.5(b)), the two mechanisms at play that store and transfer energy periodically between each other are the electric field between the capacitor's plates and the magnetic field enclosed by the inductor's windings. For such a system, resonance happens when the circuit is driven at the following frequency:

$$f_0 = \frac{1}{2\pi\sqrt{LC}} \quad (2.8)$$

At f_0 , the system's inductive and capacitive reactances cancel each other out so that only the real resistance of the network limits the flow of electrical energy, consequently, at resonance the source voltage and current are perfectly in phase with each other, while the voltage waveforms of the resonating inductor and capacitor are out of phase for series resonance, and the currents are out of

phase for parallel resonance.

If a resistive load is connected to the network, it will damp the system by dissipating power every cycle. Even when an actual discrete load is not connected to a resonant network, it will experience damping due to the distributed resistance associated with the interconnecting conductors and element leads. The quality factor that results from intrinsic losses, such as the equivalent series resistance (ESR) of an inductor is called the intrinsic quality factor, Q_i , whereas the quality factor resulting from the addition of a discrete resistive load is called the loaded quality factor, Q_l .

Figure 2.5(c) shows the standard frequency response of an RLC network for various loading conditions. For the series RLC (SRLC) topology the plot may be interpreted as the network's voltage gain Vs. frequency. On the other hand, for the parallel RLC topology (PRLC) the plot may be understood as the network's current gain Vs. frequency. As the network's Q is increased, the 3-dB BW is reduced, resulting in a much tighter regime of resonant operation. In a SRLC network, the current through the resonant tank is boosted by a amount equal to the Q factor, whereas for the PRLC network it is the voltage across the resonant tank that is scaled by Q .

When a SRLC circuit is operated above its resonance frequency, the inductance will dominate, and the network will look like an equivalent inductive reactance to the source driving it. The equivalent inductance of the foregoing inductive reactance will be smaller than the actual physical inductance. On the other hand, if the network is driven below resonance, then the capacitance will dominate and it will look like an equivalent capacitive reactance at the terminals. Because the PRLC circuit is the dual of the SRLC, the foregoing behavior will be inverted, such that when the circuit is driven below resonance it looks like an inductor, and when it is driven above it looks like a capacitor

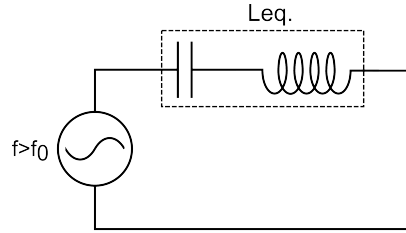


Figure 2.6: Partial Series Compensation

The addition of a capacitor in series with an inductor and deliberate operation above resonance so as to reduce or trim the overall inductive reactance to some smaller value is called partial series compensation, and the equivalent inductance that results can be expressed as:

$$L_{eq} = L - \frac{1}{\omega^2 C_s} \quad (2.9)$$

Partial series compensation is often used in IPT systems with parallel resonant topologies so as to trim the primary and/or secondary coil self-inductance to some lower value that is then resonated with a parallel capacitor [50, 28].

The quality factors and network impedance for parallel and series resonant networks are summarized in Table 2.1:

Table 2.1: RLC Network Attributes

	SRLC	PRLC
Impedance	$Z = j\omega L + \frac{1}{\omega C} + R$	$Z = j\omega L + \frac{1}{\omega C + \frac{1}{R}}$
Quality Factor	$Q_s = \frac{\omega L}{R}$	$Q_p = \frac{R}{\omega L}$

From the foregoing definitions of electrical resonance it can be readily seen that it is a very desirable property for use in loosely coupled IPT systems where there exists a need to completely tune-out the large inductive reactances that arise at the primary and secondary due to correspondingly large stray fields. To summarize, resonance achieves the following key objectives in loosely coupled IPT systems:

1. Reduces the volt ampere (VA) rating of the primary power supply [51].
2. Reduces the VA rating of the secondary power electronics [4].
3. Boosts the power available at the secondary by an amount equal to the secondary tuned Q [20].
4. Reduces switching losses for soft-switched power electronic schemes as will be detailed in chapter 4 [10].

2.3 Electrical Model of Loosely Coupled IPT Systems

While the design of the inductive structures that couple power magnetically is largely done in the electromagnetics realm via FEA software, the design of the source and receiver side power electronics requires an electrical model that links the EM regime to the lumped element electrical one; accordingly, two models may conceivably be used for the stated purpose, the standard mutual inductance model (M-model), or the conventional transformer model (T-model) [22].

The T-model uses the concepts of transformed voltage and reflected current to describe the magnetic coupling through the transformer windings. Both the transformed voltage and reflected current are defined by the transformer's windings turns ratio. The rigorous use of the T-model requires that the magnetizing/coupling inductance and the primary and secondary leakage inductances be separated for circuit analysis, which makes the analysis process challenging and the resulting expressions complex. This model is therefore usually better suited for the analysis of standard transformers that are tightly coupled, because their associated leakage inductances are generally very small in comparison with their magnetizing inductance and can therefore be neglected altogether so as to yield simpler analysis and corresponding expressions.

On the other hand, the M-model uses the concepts of induced and reflected voltages to describe the magnetic coupling between two inductors, and does not require the magnetizing and leakage inductances to be separated for circuit analysis. Both the induced and reflected voltages are defined in terms of the mutual inductance of the coupled inductors. Because in loosely coupled IPT systems

the leakage inductances are significantly greater than the magnetizing inductance, they cannot be neglected, hence the M-model is much better suited for the analysis and design of loosely coupled IPT systems. In addition to being easier to deal with analytically, the M-model is also advantageous in that it allows for the design of the primary and secondary power electronics to be carried out independent of each other provided that the mutual inductance over the system's range of operation is known.

Because of its ease of use and stated advantages, the work undertaken in this thesis will rely on the M-model. The next sections will summarize the mathematical relationships that are most relevant to this work based on the M-model.

2.3.1 Mutual Inductance Circuit Model

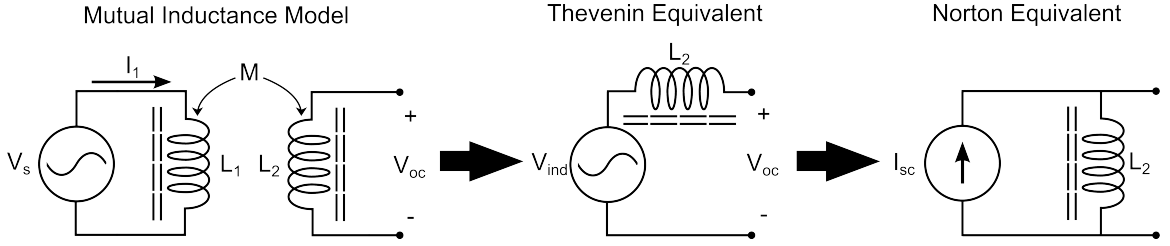


Figure 2.7: Mutual Inductance Circuit Model (M-model)

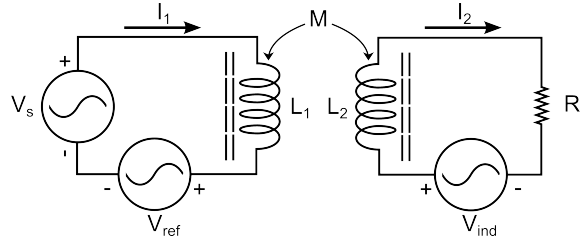


Figure 2.8: M-model of Uncompensated IPT System with Resistive Load

With reference to Fig.2.7, the induced open circuit voltage, V_{oc} , across the terminals of a secondary coil, L_2 , coupled to a primary coil, L_1 , through a mutual inductance, M , is given by:

$$V_{oc} = j\omega M I_1 \quad (2.10)$$

This relationship allows for easy experimental measurement of M , as both V_{oc} and I_1 can be measured with an oscilloscope, resulting in the following expression:

$$M = \frac{V_{oc}}{\omega I_1} \quad (2.11)$$

The mutual inductance is related to the coupling coefficient of the coupled inductors by the following standard relation:

$$k = \frac{M}{\sqrt{L_1 L_2}} \quad (2.12)$$

Using the Norton equivalent circuit at the secondary side, the short circuit current, I_{sc} , that flows through L_2 , is expressed as:

$$I_{sc} = \frac{V_{oc}}{j\omega L_2} = \frac{MI_1}{L_2} \quad (2.13)$$

The maximum reactive power that may be transferred over an air gap by a system of coupled coils with no resonant tuning is given by the product of V_{oc} and I_{sc} as [20]:

$$S_u = \omega I_1^2 \frac{M^2}{L_2} \quad (2.14)$$

The maximum active power that can actually be delivered to a resistive load connected to the secondary coil in such a system (Fig.2.8) is obtained when the load is matched to the coil's reactance, and ends up being only half of S_u ; for many applications, this is not enough, thereby requiring resonant tuning to achieve enhanced power transfer.

Figure 2.8 also highlights that when a current flows in the secondary coil, it reflects a voltage back to the primary coil that has the opposite polarity of the primary source voltage, V_s :

$$V_{ref} = -j\omega M I_2 \quad (2.15)$$

2.3.2 Mathematical Model of IPT System With Parallel Resonant Secondary

In most of the wireless EV charging systems presented in section 1.2, the parallel resonant topology has been chosen for the secondary. While there are other topologies that may be used, the parallel secondary architecture is beneficial for battery charging because of its constant current source characteristics [51, 52, 37, 50].

The delivery of power to an EV battery pack requires stable DC voltage and current. While there are a number of power processing methods that can achieve the conversion of AC power to regulated DC power, the simplest one is the use of a high frequency (HF) full-bridge (FB) rectifier with an output LC-filter between the resonant tank and the load. This scheme is often preferred because it simplifies the system integration on the vehicle side, thereby reducing size, complexity, and cost. To achieve stable power flow and regulation with the foregoing approach, the primary side power electronics is relied upon for execution of closed loop control [53, 40].

In view of the aforesaid, the work undertaken in this thesis uses the parallel resonant secondary topology along with a HF-FB rectifier with LC-filter.

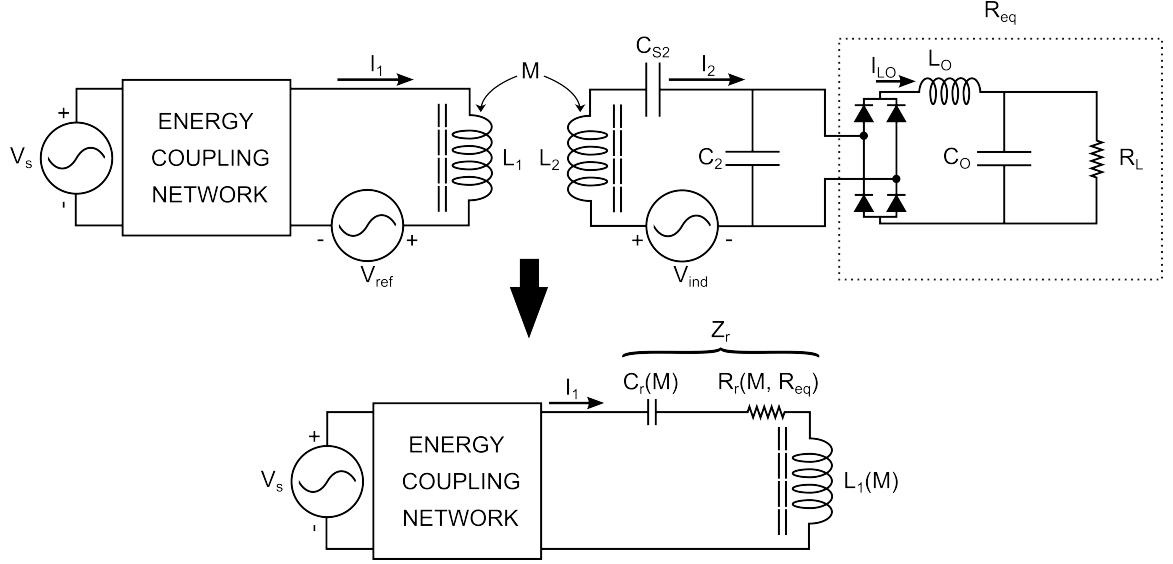


Figure 2.9: M-model of Resonant IPT and its Equivalent When the Secondary is Referred to the Primary

With respect to Fig.2.9, provided that the output inductor, L_o , is large enough to ensure continuous conduction of the rectifier diodes over the system's full range of operation, then the following relation holds true [37]:

$$R_{eq} = \frac{\pi^2 R_L}{8} \quad (2.16)$$

As previously stated, the analysis and design of IPT systems may be carried out at the primary or secondary. A design that is focused on the secondary side, may be easily carried out by simply using the Thevenin and/or Norton equivalents introduced in Fig.2.7. Conversely, a design that is focused on the primary may be carried out by simply reflecting the secondary to the primary.

As illustrated in Fig.2.9, when a parallel resonant secondary is reflected to the primary, it presents an impedance, Z_r , to the primary power supply. The real part of Z_r , is a function of the variable mutual inductance and of the load. The variability in M results from changes in alignment between the coils, while the variability of the load is due to changes in the battery's voltage and current profiles as it charges. On the other hand, the imaginary part of Z_r is only a function of M , and is capacitive in nature [1].

The capacitor C_{S2} in Fig.2.9 is used for partial series compensation of the secondary coil so as to reduce its reactance. In a practical design, the use of partial series compensation on the secondary coil may serve one or both of the following purposes: 1) reducing the VA rating of the components connected to the resonant tank, and/or 2) boosting the current out of the secondary coil, thereby enhancing its power delivery capabilities. The later function is often carried out during the physical implementation's fine-tuning stage, where there is often a need to increase I_2 to achieve the design's target power level, but the pick-up coils magnetic characteristics have already been largely fixed by its construction. It is relevant to mention that for the parallel secondary topology, the maximum load

current that may be delivered without use of partial series compensation occurs when the pick-up is perfectly tuned and is equal to I_{sc} .

When partial series compensation is applied to the parallel secondary, three different quality factors can be defined [50, 28, 37]. The first one is known as the voltage boost quality factor, and is defined as:

$$Q_{2v} = \frac{R_{eq}}{\omega L_{2eq}} \quad (2.17)$$

where L_{2eq} is the equivalent secondary coil's inductance after application of partial series compensation:

$$L_{2eq} = L_2 - \frac{1}{\omega^2 C_{s2}} = \frac{\omega^2 L_2 C_{s2} - 1}{\omega^2 L_2 C_{s2}} \quad (2.18)$$

Q_{2v} is the conventional quality factor that was defined for the PRLC topology in section 2.2.3 (Table 2.1). The second quality factor that may be defined is known as the current boost quality factor:

$$Q_{2i} = \frac{C_2}{C_{s2}} + 1 \quad (2.19)$$

Q_{2i} is used to quantify the increase in I_2 from its uncompensated value, I_{sc} , to its compensated value, $Q_{2i} \times I_{sc}$. The amount of partial series compensation that may be carried out as quantified by Q_{2i} has been reported as being limited to less than 3 because of the added sensitivity to the overall resonance in the pick up coil (i.e. due to component aging), as well as because of saturation of the pick-up coil ferrite that results from the increased flux density [50, 28]. A Q_{2i} of 1 results when C_{s2} is increased without bound, which is equivalent to no compensation because the resulting capacitive reactance is negligible.

The third quality factor that may be defined, is the secondary's overall quality factor, which takes into account the effect of both Q_{2i} and Q_{2v} ; this later quality factor is defined as:

$$Q_{2t} = Q_{2v} \times Q_{2i} \quad (2.20)$$

For practical designs, Q_{2t} is limited to being less than 10 [4, 20], and for most of the high power EV charging systems presented in section 1.2 it is less than 6. This limitation in the overall secondary Q is due to the challenges that arise in controlling the system due to the narrower system BW at higher values of Q_{2t} . Another factor that dictates the limit imposed on Q_{2t} is the need to maintain the secondary's VA ratings within the limits prescribed by governing standards such as UL.

L_{2eq} may also be expressed in terms of the three quality factors that result from the application of partial series compensation as:

$$L_{2eq} = \frac{R_{eq}}{\omega Q_{2v}} = \frac{R_{eq} Q_{2i}}{\omega Q_{2t}} \quad (2.21)$$

Application of standard circuit analysis on the circuits of Fig.2.9 results in a secondary impedance given by:

$$Z_2 = \frac{R_{eq}(\omega L_{2eq})^2}{R_{eq}^2(1-\omega^2 C_2 L_{2eq})^2 + (\omega L_{2eq})^2} + j \frac{\omega L_{2eq} R_{eq}^2 (1-\omega^2 C_2 L_{2eq})^2}{R_{eq}^2(1-\omega^2 C_2 L_{2eq})^2 + (\omega L_{2eq})^2} \quad (2.22)$$

The reflected impedance seen at the primary can be shown to be:

$$Z_r = \frac{V_{ref}}{I_1} = \frac{(\omega M)^2}{Z_2} = \frac{R_{eq}(\omega M)^2[\omega^2 C_2 L_{2eq} - (\omega^2 C_2 L_{2eq} - 1)]}{R_{eq}^2(\omega^2 C_2 L_{2eq} - 1)^2 + (\omega L_{2eq})^2} - j \frac{\omega^3 M^2 [C_2 R_{eq}^2 (\omega^2 C_2 L_{2eq} - 1) + L_{2eq}]}{R_{eq}^2(\omega^2 C_2 L_{2eq} - 1)^2 + (\omega L_{2eq})^2} \quad (2.23)$$

Consequently, the equivalent reflected resistance and capacitance that appear in series with the primary coil self-inductance in Fig.2.9 are given by:

$$R_r(M, Req) = Re\{Z_r\} = \frac{R_{eq}(\omega M)^2[\omega^2 C_2 L_{2eq} - (\omega^2 C_2 L_{2eq} - 1)]}{R_{eq}^2(\omega^2 C_2 L_{2eq} - 1)^2 + (\omega L_{2eq})^2} \quad (2.24)$$

$$C_r(M) = [\omega Im\{Z_r\}]^{-1} = \left[-\frac{\omega^4 M^2 [C_2 R_{eq}^2 (\omega^2 C_2 L_{2eq} - 1) + L_{2eq}]}{R_{eq}^2(\omega^2 C_2 L_{2eq} - 1)^2 + (\omega L_{2eq})^2} \right]^{-1} \quad (2.25)$$

The power that is thus delivered to the reflected load is given by:

$$P = Re\{I_1^2 Z_r\} = I_1^2 R_r = \frac{R_{eq}(\omega M I_1)^2[\omega^2 C_2 L_{2eq} - (\omega^2 C_2 L_{2eq} - 1)]}{R_{eq}^2(\omega^2 C_2 L_{2eq} - 1)^2 + (\omega L_{2eq})^2} \quad (2.26)$$

If the system is operated at or close to the secondary's resonant frequency:

$$\omega_0 = \frac{1}{\sqrt{L_{2eq} C_2}} \quad (2.27)$$

the term $(\omega^2 L_{2eq} C_2)$ will be equal or very close to one. When this happens equations (2.23) and (2.26) become:

$$Z_r = \frac{\omega_0 M^2 Q_{2v}}{L_{2eq}} - j \frac{\omega_0 M^2}{L_{2eq}} \quad (2.28)$$

$$P = \frac{\omega_0 M^2 I_1^2 Q_{2v}}{L_{2eq}} \quad (2.29)$$

Equation (2.29) is conventionally known as the IPT power equation, and it is deemed by many authors as the starting point for the design of a resonant IPT system [37, 1, 4].

To complete the work of this thesis, the design and construction of a full IPT system was undertaken. This required a complete understanding of the mathematical relationships that govern the operation of the secondary side. Consequently, the following are the expressions for the voltage and current for all secondary side resonant tank components:

$$I_2 = \frac{R_{eq}}{j\omega L_{2eq} + R_{eq}(1 - \omega^2 L_{2eq} C_2)} \frac{M I_1}{L_{2eq}} \quad (2.30)$$

$$I_{C2} = \frac{-R_{eq} \omega^2 L_{2eq} C_2}{j\omega L_{2eq} + R_{eq}(1 - \omega^2 L_{2eq} C_2)} \frac{M I_1}{L_{2eq}} \quad (2.31)$$

$$V_{L2} = \frac{\omega R_{eq} L_2}{\omega L_{2eq} - j R_{eq}(1 - \omega^2 L_{2eq} C_2)} \frac{M I_1}{L_{2eq}} \quad (2.32)$$

$$V_{Cs2} = \frac{-R_{eq}}{\omega^2 L_{2eq} C_{s2} - j\omega R_{eq} C_{s2} (1 - \omega^2 L_{2eq} C_2)} \frac{MI_1}{L_{2eq}} \quad (2.33)$$

$$V_{C2} = \frac{\omega R_{eq} L_{2eq}}{\omega L_{2eq} - jR_{eq} (1 - \omega^2 L_{2eq} C_2)} \frac{MI_1}{L_{2eq}} \quad (2.34)$$

Expressions for the voltage and current ratings of all primary side components will be presented in chapter 4, which focuses on the design of the primary power supply.

Before the mathematical model presented thus far can be used to design the electrical system components, all key magnetic attributes of the coupled coils to be used must be fully known. Accordingly, the next chapter will detail the design, construction, and experimental characterization of the magnetic pads used for this work.

Chapter 3

Magnetic Pad Design

3.1 Archimedean Spiral Coils

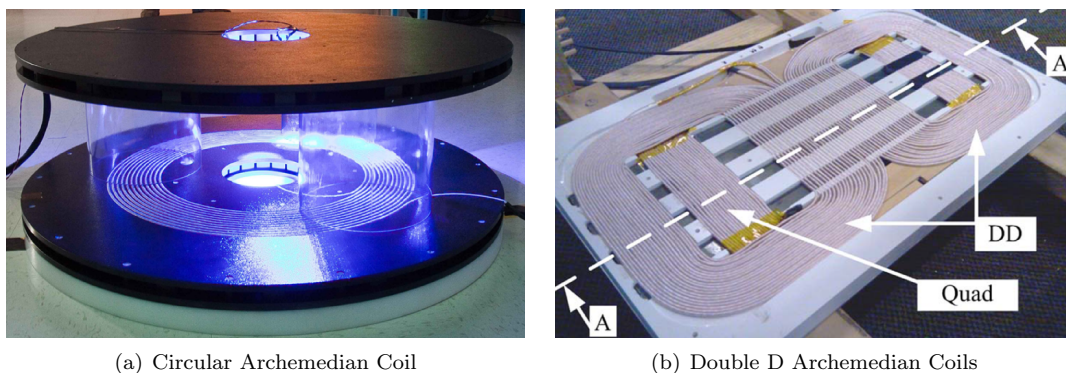


Figure 3.1: Planar Archimedean Coils

The first step in the design of an inductive power transfer system is the selection of a suitable inductive structure geometry from a number of available choices [4, 51, 54]. Once a geometry that best suits the target application has been selected, then a thorough FEA based EM optimization of the design is undertaken prior to fabricating it. The goals of the FEA optimization/simulation are [16, 17, 18, 55, 28, 26, 27]:

1. Achieving the highest possible values of mutual inductance and magnetic coupling over the system's target range of positional operation.
2. Reducing the design's physical size and material cost as much as possible without compromising its power transfer capabilities.
3. Achieving self-inductance values that will ensure coil voltage levels that are within established UL safety regulations.
4. Ensuring regulatory compliance with the established field emission standards (ICNIRP).

5. Having a complete understanding of how all key magnetic attributes vary over the system's range of positional operation so as to properly design the primary and secondary power electronics in terms of component ratings and closed loop control.

Figure 3.1 shows two of the coil geometries most commonly used in wireless EV charging systems [56, 16, 17]. These geometries are broadly known as flat Archimedean spirals. To date Archimedean coils are the preferred choice for a number of applications because of their small volumetric footprint, and their single-sided flux profile when used with a ferrite backplane. The first geometry, Fig.3.1(a), is a standard circular geometry; the second geometry, Fig.3.1(b), is known as a double-D (DD) geometry and it is essentially two coplanar semicircular Archimedean coils placed side-by-side and connected electrically in parallel (i.e. magnetically in series).

Despite having lower coupling and mutual inductance profiles than similarly sized DD coils over identical air gaps and misalignment, for static EV charging applications, the circular geometry is still the most widely used. This is due to its ease of manufacture, lower material cost, symmetric coupling profile, ease of experimental characterization, and very well understood magnetic characteristics.

A noteworthy feature of circular Archimedean coils is that identically sized coil pairs possess a null in their mutual inductance profile which is fixed at a misalignment distance approximately equal to 70% of the coil's central diameter regardless of their separation. The existence of this null in the coupling profile is important because it sets a boundary in the effective area over which a given amount of power may be transferred for a given maximum operational value of Q_{2t} and I_1 . The mechanism that causes the null to occur is often referred to as flux cancellation. Flux cancellation essentially means that equal amounts of flux enter the pad through the top and bottom of the plane of the secondary coil, thereby canceling each other out and resulting in zero induced voltage[16].

For misalignment distances greater than 70% of the coil's diameter the mutual inductance goes negative. This inversion in the sign of M is readily seen in an oscilloscope as a 180 degree phase shift in the voltage induced at the terminals of the secondary. This phase-shift is explained by the fact that past the null the induced voltage is caused by the flux that enters the coil through the top of the secondary coil instead of the bottom. It is also noteworthy that the negative mutual inductance reaches a minimum and then tapers off to zero as the misalignment distance is increased further.

In general, the self and mutual inductance of circular Archimedean coils are governed by the following variables: the number of turns, the distance between turns (also known as pitch), the coil's central diameter, and the use of flux shaping materials such as Ferrite. Accordingly, an increase in the number of turns, will result in an increase in the self and mutual inductance. An increase in the coil's central diameter will result in a shift of the characteristic null in the coupling profile further out, resulting in a larger charging zone, but if the increased central diameter is not accompanied with a corresponding increase in the number of turns, then the mutual inductance will decrease, effectively reducing the maximum power available over the expanded charging zone. In [16, 17, 27] it is shown that an increase in pitch decreases the mutual inductance. The physical reason why the mutual inductance decreases with increasing pitch is that the flux collapses in between the gaps at smaller radial distances from the coils center thereby reducing the coil's magneto motive force (MMF). In contrast with the mutual inductance, the coupling coefficient tends to increase as the

winding is spread out over the area of the coil, resulting in a trade-off between the two design variables.

Because the focus of this thesis was the design of the primary side power electronics, the approach taken in the design of the magnetic pads was to forgo the initial FEA based optimization process, which in itself could be the subject of a thesis, and instead construct the pads so as to replicate some of the better designs showcased in the literature. The insights obtained from the literature review carried out and previously summarized were relied upon when designing the physical implementation. Once the coils were built their magnetic attributes were experimentally measured and used to carry out the design of the primary and secondary side power electronics

3.2 Coil Fabrication

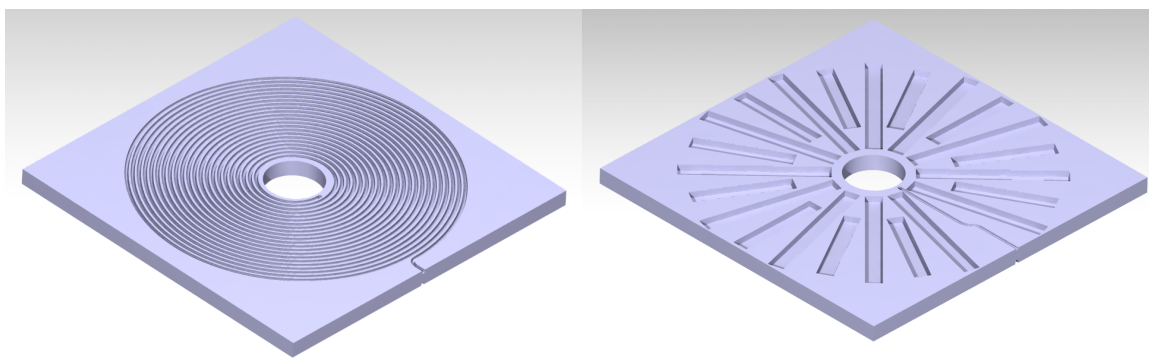


Figure 3.2: Catia V5 Mechanical Drawing of Magnetic Pads

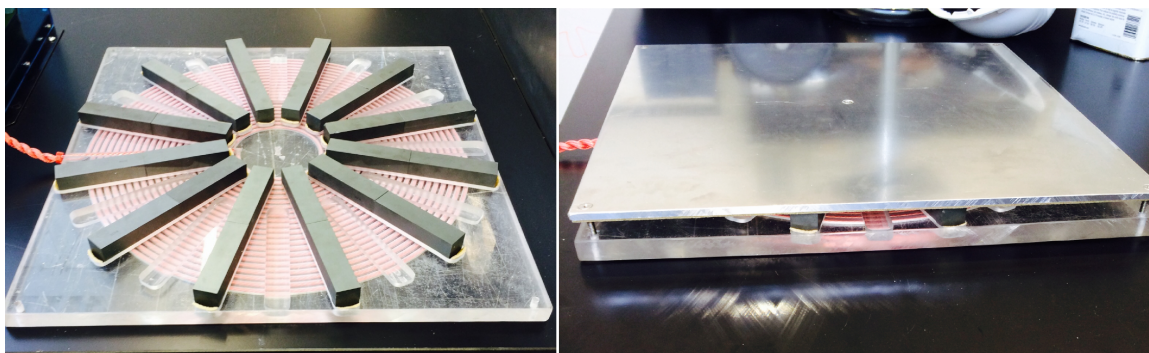


Figure 3.3: Constructed Magnetic Pads

The physical design of the magnetic pads was completed by means of Catia V5 mechanical design software so as to ensure accurate physical dimensions and a professional finish. Accordingly, the shape of the coil was drawn on a 25.4 mm by 558 mm by 558 mm solid volume (Fig.3.2). On one plane a grooved channel in the shape of a 22 turn circular Archimedean spiral was drawn. On the opposite plane a total of 22 rectangular pockets were placed for housing field shaping ferrite spokes. The addition of a backplane of high permeability ferrite spokes was carried out so as to shape the returning flux and thereby constrain its flow to the small region lying immediately behind the plane

of the coil where the Ferrites were placed. This field shaping method is responsible for giving the circular Archimedean coil its characteristic single sided flux profile.

Using the CAD file obtained from Catia V5 the coil was fabricated using a CNC milling machine. The material used for the construction was a clear Polycarbonate sheet having the previously stated dimensions. The coils were designed so as to have known initial self-inductances of $125\mu\text{H}$ with the aid Wheeler's formula for air-core Archimedean coils (3.1) [57], and their actual values were measured using an inductance/capacitance/resistance (LCR) meter. This initial design value for the self inductance served only as a baseline, as it would later be increased due to the addition of the ferrite spokes.

$$L_w = \frac{31.33\mu_0(rN)^2}{8r+11w} \quad (3.1)$$

$$w = kN \quad (3.2)$$

$$r = 0.5(I.D. + kN) \quad (3.3)$$

$$k = \text{pitch} + \text{wirediameter} \quad (3.4)$$

To further enhance the magnetic performance, durability, and look of the design, an Aluminum (Al) backplane was placed (fastened with flush mounting screws) behind the Ferrite spokes, effectively sandwiching the spokes between the Polycarbonate coil former and the Al backplane. The foregoing Al sheet had the primary purpose of canceling any stray fringe fields that escaped being shaped by the Ferrite. The canceling effect is achieved by virtue of the fact that the currents induced on the high conductivity Al sheet will themselves produce fields that oppose the leakage fields and thereby cancel them [16]. The Al backplane also served the purpose of firmly fastening the ferrite spokes to the Polycarbonate structure while also protecting them from mechanical shock. This later objective was achieved by placing a sheet of foam padding between the Polycarbonate pockets and the Ferrites, as well as one between the Al sheet and the Ferrites. Figure 3.3 shows the constructed pads.

3.3 Experimental Characterization of Coil Attributes

$$P_{loss} = \frac{IV}{Q_i} \quad (3.5)$$

The nominal attributes of the coils built are listed in Table 3.1. The self inductance was measured using an LCR meter, and the AC power loss of the pad as a result of skin effect is defined by equation (3.5) where I and V are the nominal operating pad input voltage and current at rated power, and Q_i is the coil's intrinsic quality factor defined with respect to its AC resistance at the target operating frequency.

For precise measurement of the pads' mutual inductance, coupling coefficient, coupled self-inductances, and uncompensated power over their range of positional operation, the coupled pad's must be energized with a known primary current and then the required measurements are taken while the pads are misaligned in the vertical and/or horizontal directions in small steps. When the resulting measurements are plotted as a function of the vertical and horizontal offsets, the resulting plot is a

Table 3.1: Nominal Magnetic Pad Attributes

Attribute Name	Value/Dimension/Material
Number of Turns (N)	22
Outer Diameter (O.D.)	482.6 mm
Inner Diameter (I.D.)	101.6 mm
Pitch (p)	3 mm
Conductor Diameter (d)	5.84 mm
Inductance (L_{avg})	172.6341 μH
Resistance (R_{ac})	160 m Ω
Quality Factor (Q_i)	200
Power Loss (P_{loss})	135 W
No. of Ferrite Spokes	12
Ferrite Material	Ferroxcube 3C94
Litz Conductor	Type II (16AWG 4x5X24/36)

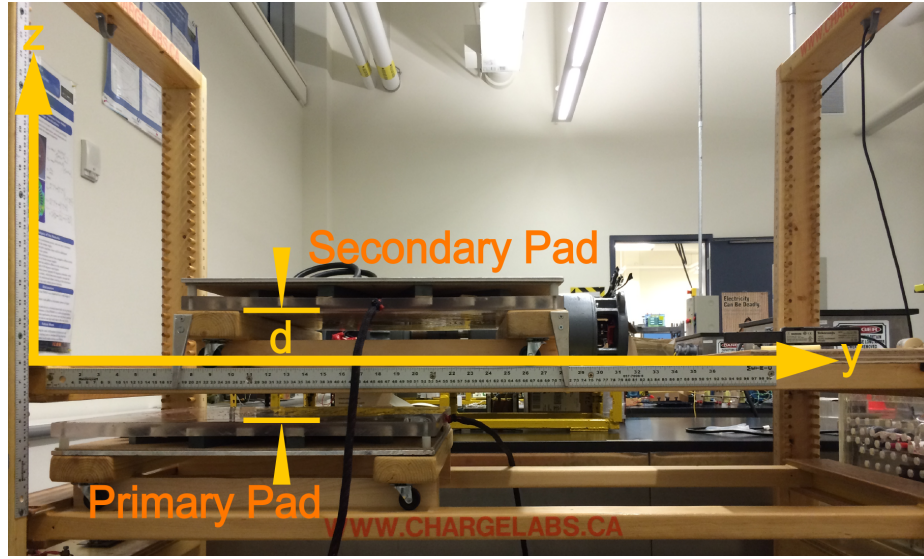


Figure 3.4: Experimental Test Bench for Measurement of Pad Attributes

profile of the coupled coils' magnetic attributes. In order to make very precise measurements of the foregoing characteristics over the full range of coil-to-coil separation and misalignment distances the test bench shown in figure 3.4 was constructed.

To energize the primary coil a phase-shifted full-bridge inverter with a series compensation capacitor was used. The value of the tuning capacitor was chosen according to the procedure outlined in [10]. The capacitor was chosen so as to operate the system slightly above resonance and thereby maintain a slightly inductive mode of operation so as to ensure zero voltage switching (ZVS) of the bridge semiconductors.

The mutual inductance was obtained by measuring the secondary's open circuit voltage and the primary's current. With these two measurements the mutual inductance is readily obtained with the aid of equation (2.11). The coupling coefficient was obtained by two separate methods. The first method applied was the measurement of the primary coil voltage and secondary coil's open circuit voltage so as to use the voltage transfer ratio V_{2oc}/V_1 as a measure of k . The second method

used was the utilization of equation (2.12) along with the measured mutual and self-inductance to compute k . Both methods produced very similar results. The uncompensated reactive power (S_u) transfer capability of the pads was obtained by measuring the short-circuit current of the secondary pad and then taking the product of it and V_{2oc} . Finally, the coupled coil self-inductances were measured at each point along horizontal offset trajectory by means of an LCR meter.

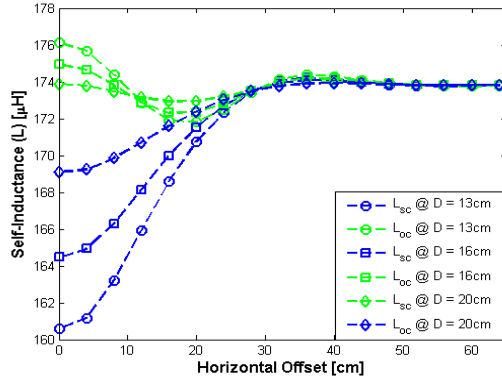
Figure 3.5 shows the resulting characteristics of the pads measured magnetic attributes over a range of axial misalignment spanning 64 cm for three separate coil-to-coil separation distances, namely: 12 cm, 16 cm, and 20 cm.

The first characteristic, Fig.3.5(a), shows the profile of the coupled pads self-inductances for two different conditions: 1) a shorted secondary pad (L_{sc}), and 2) an open secondary pad (L_{oc}). The measurements are taken with the LCR meter on one pad, while the other one coupled to it has its terminals either shorted or opened. The reason why the two conditions are considered is that depending on the resonant topology chosen for the primary and secondary networks, the self-inductance may behave differently [38]. For example, for the parallel resonant topology, the pad's self-inductance varies according to the short-circuit measurement profile, while for the series resonant topology the inductance varies according to the open circuit measurement profile.

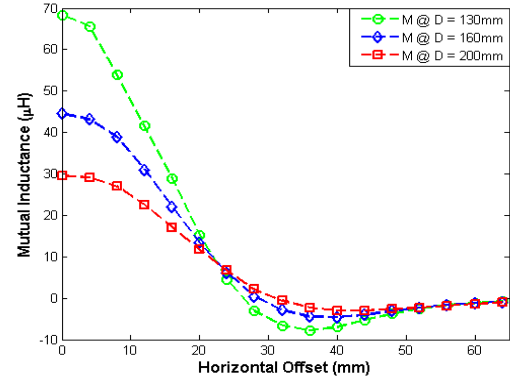
The plots of mutual inductance and coupling verify the existence of the fixed characteristic null in the pads magnetic profile, as well as the previously described behaviour beyond it. Another noteworthy observation is that L_{sc} and L_{oc} both converge to a common value as the pads are decoupled, with the convergence starting around the characteristic null point.

The last plot, Fig.3.5(d), shows the effect that the primary current has on the overall power transfer ability of the coupled coils.

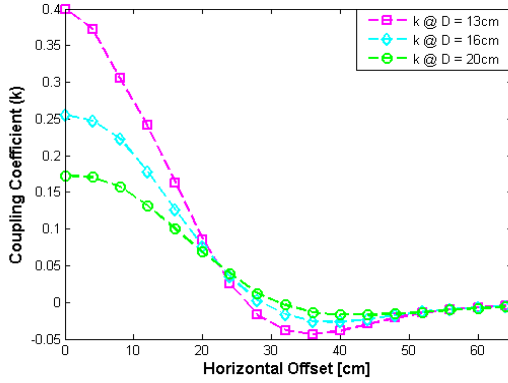
With all of the foregoing characteristics in hand, the design of the primary and secondary power electronics can now be undertaken. The next chapter will address this topic.



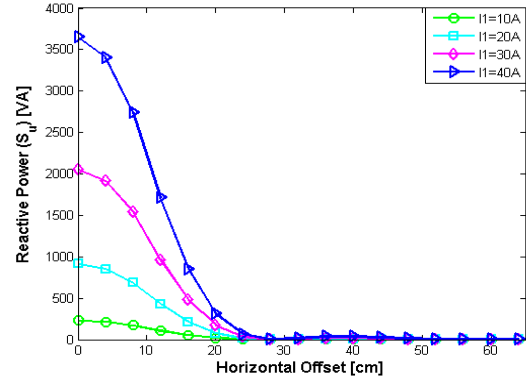
(a) Coupled Self Inductances Vs. Alignment



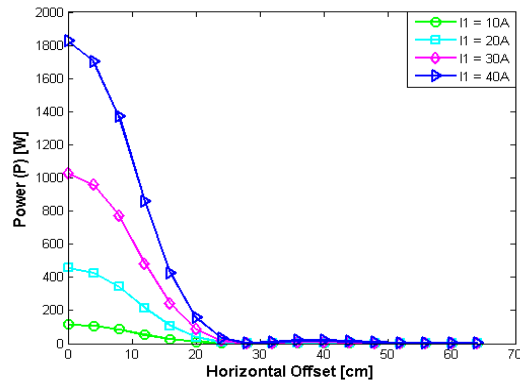
(b) Mutual Inductance Vs. Alignment



(c) Uncompensated Reactive Power Vs. Alignment



(d) Uncompensated Reactive Power Vs. Alignment



(e) Uncompensated Active Power Vs. Alignment

Figure 3.5: Measured Pad Attributes

Chapter 4

Primary Side Power Supply Design

4.1 EV Charging Power Supply Topologies

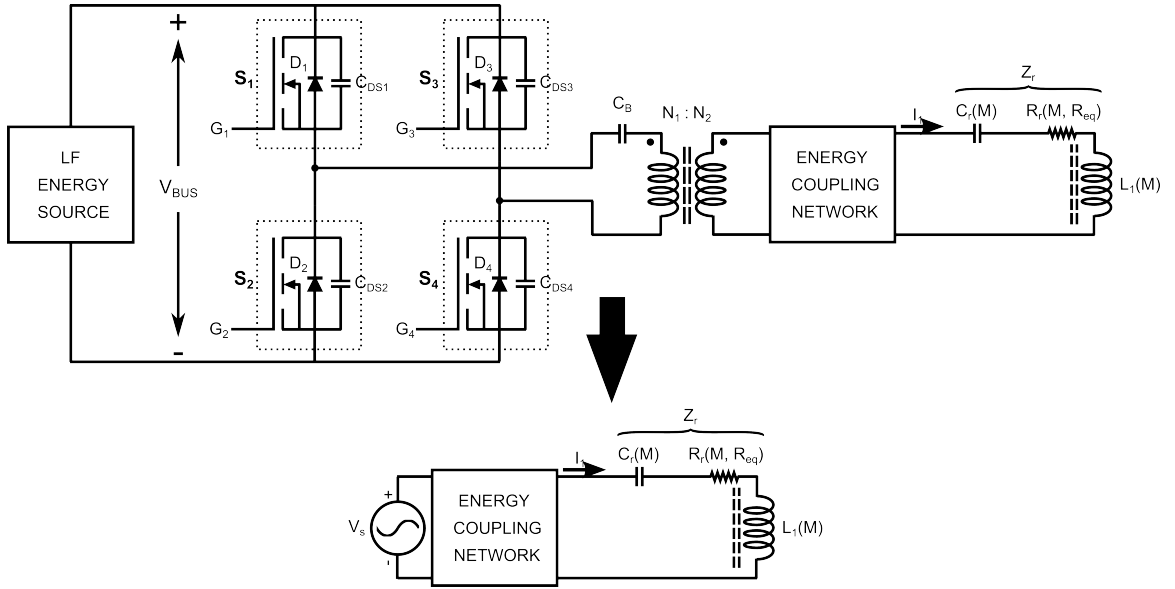


Figure 4.1: Switching Network and its Equivalent

As highlighted in section 1.2, the majority of modern wireless EV charging power supplies are implemented using one of two common architectures: the series LC resonant (SLC) or the hybrid series-parallel LC resonant (LCL) topology [32, 58, 37, 59, 33].

As shown in Figure 4.1, the two topologies share a common power electronics switching network. The switching network is generally a voltage fed, full-bridge (FB) made up of four power semiconductors that are commutated so as to invert the incoming DC energy and thereby produce a HF square wave. A number of gate-drive switching patterns can be used to generate the desired inverter output, but the preferred one for IPT applications is the phase-shifted (PS) scheme. Figure 4.2 shows an example of the logic switching pattern that would result in PS operation. The series switch pairs are said to

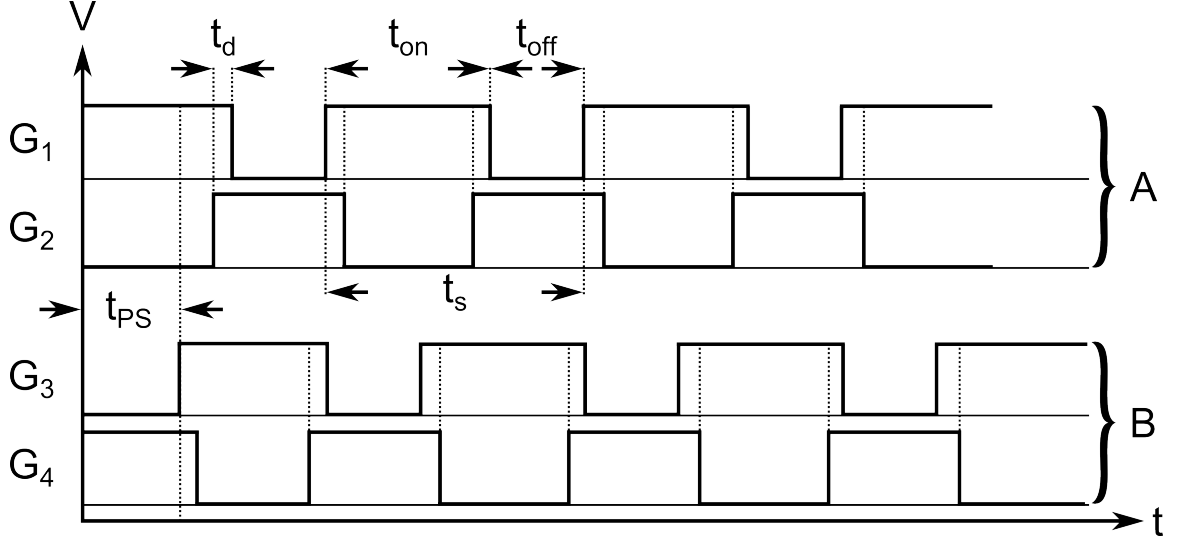


Figure 4.2: Phase-Shift Control Waveforms

make up one leg of the two inverter legs, such that switch pairs $S_1 - S_2$ and $S_3 - S_4$ make up legs A and B respectively. By modulating the value of t_{PS} , the power flow of the system can be regulated. It is relevant to note that for a t_{PS} corresponding to 180 degrees PS, the switching network behaves as a standard anti-parallel-switch commutated inverter. The small time period, t_d , between the rising and falling edges of the gate drive signals of switch pairs in the same leg ($S_1 - S_2, S_3 - S_4$) is necessary so as to ensure that at no time both switches on a given leg are turned on simultaneously, as this would result in a shorting of the DC-bus and an immediate catastrophic failure of the bridge.

Because the resonant networks that are connected to the output of the FB have significant filtering capability due to their sharply tuned band-pass frequency response, which is nominally centered at f_0 , the system may be simplified during the design phase by assuming a sinusoidal voltage source, v_S , with operating frequency of f_0 [38].

$$v_S = V_S \times \sin(2\pi f_0 t) \quad (4.1)$$

The peak amplitude of v_S is related to the FB's DC-bus input voltage, V_{DC} , and the PS control angle, θ_{PS} , as follows:

$$V_S = \frac{2\sqrt{2}V_{DC}}{\pi} \sin\left(\frac{\theta_{PS}}{2}\right) \quad (4.2)$$

Both power supply topologies also share the common requirement of having a HF isolation transformer interfacing the output of the FB and the input to the resonant tank [60, 53]. This requirement is imposed by regulatory safety standards such as UL1557, IEC1558, and EN61558. This isolation transformer requires core anti-saturation protection, so a DC blocking capacitor is normally placed in series with it on the FB side. The possibility of core saturation arises because the switch turn-on and turn-off times in the switching network are in practice never truly identical (i.e. due to inherent variability in the production spread of the semiconductors, their response times may vary from each other). The foregoing small variations in the turn-on/off times can conceivably result in the build

up of DC energy at the core over several switching cycles. As will be shown in section 4.1.3, the isolation transformer's parasitic attributes can be used constructively to complete the resonant tank in the case of the LCL topology, thereby achieving a reduction in the number of discrete energy storage elements required, and by extension reducing the overall system component count and cost.

The design of the primary power supply calls for the following choices to be made:

1. Selection of the FB switching frequency, f_s .
2. Selection of the resonant energy coupling network (ECN) topology to be used.
3. Sizing of the energy storage element values (i.e. capacitances and inductances) that make up the ECN so as to ensure the desired resonant operating mode.
4. Selection of the FB semiconductors and their associated gate-driver scheme.
5. Selection of the FB switching control strategy.
6. Determination of the appropriate ratings (with a suitable safety margin) for all of the aforesaid components; this includes the peak voltage and current, peak power, and dynamic response speed (the later is for the semiconductors).

Before the above listed choices can be made for the power supply the following items must already be known:

1. Maximum power transfer level, P_{max} .
2. Nominal operating frequency.
3. Magnetic pad characteristics: k_{min} , $M(k_{min})$, $L_{sc}(k_{min})$, and $L_{oc}(k_{min})$.
4. Secondary side ECN topology and storage element values.
5. Nominal load value, R_{eq} .
6. Nominal value of the three secondary quality factors: Q_{2t} , Q_{2v} , and Q_{2i} .
7. The peak DC bus input voltage of the inverter, V_{DC}

For this work, the above stated specifications are shown in Table 4.1. The power level was selected so as to operate the charger as an equivalent SAE Level II charger. The nominal operating frequency was set at 30 kHz instead of the 85 kHz prescribed by J2954 because the voltages in the ECN's become extremely high for safe operation. In order to reduce the high voltages associated with higher frequency operation it is necessary to redesign the magnetic pads so as to have smaller self-inductances. There are a number of ways to reduce the self-inductances without compromising the overall coupling of the pads. For example, the same total number of winding turns may be achieved by coil segmentation, as with a bifilar winding, resulting in several parallel connected coplanar coils, effectively reducing the equivalent inductance seen by the power supply [17, 61]. In using the foregoing approach however, it must be understood that the power supply will have to source more current; the amount of additional current required will be proportional to the number of parallel coil segments used.

Table 4.1: Nominal Design Specifications

Specification Name	Specification Value
Max Power $[P_{max}]$	3 kW
Min. Efficiency $[Eff_{min}]$	85%
Nominal Frequency $[f_0]$	30 kHz
ECN Topology	Parallel W/ Partial Series Compensation
Min. Coupling $[k_{min}]$.17
Min. Mutual Inductance $[M(k_{min})]$	30.93 μH
S.C. Secondary Inductance $[L_{2sc}(k_{min})]$	168.15 μH
S.C. Primary Inductance $[L_{1sc}(k_{min})]$	168.15 μH
O.C. Primary Inductance $[L_{1oc}(k_{min})]$	172.87 μH
Partial Series Secondary Cap. $[C_{s2}]$	0.23 μF
Parallel Secondary Tuning Cap. $[C_2]$	0.60 μF
Equivalent Nominal Load $[R_{eq}]$	17.76 Ω
Secondary Q Factor $[Q_{2t}]$	3
Voltage Boost Q Factor $[Q_{2v}]$	2.14
Current Boost Q Factor $[Q_{2i}]$	1.40
Max. DC Bus Input Voltage $[V_{DC}]$	240 V

From the given specifications the primary current needed to transfer the required power can be computed by solving equation (2.29) for I_1 :

$$I_1 = \sqrt{\frac{P_{max} L_{2eq}}{\omega_0 M^2 I_1^2 Q_{2v}}} \quad (4.3)$$

The current obtained from (4.3) serves as an initial design reference value. The final value of I_1 for the physical implementation may need to be larger in order to transfer the target power level. The need to increase the primary current upon completion and evaluation of the initial physical implementation is well reported upon in the literature [4, 16, 40, 33]. As highlighted in the cited references the VA of the tuned secondary and its short circuit current have to be large enough to support the desired power transfer level.

For this particular design, the extreme operating point is chosen to correspond to a maximum coil-to-coil air gap of 16 cm and an axial misalignment of 12 cm. This operating point corresponds to k_{min} shown in table 4.1. The magnetic design characteristics for the full operating range of coupling are shown in figure 4.3. The region to the left of the red dashed vertical line is the full operating range of coupling. The idea is to ensure that the system is able to transfer the required power at the boundary, with the understanding that if this is so, then it will also be able to do so at higher coupling points in the operating range provided that the primary current can be maintained constant.

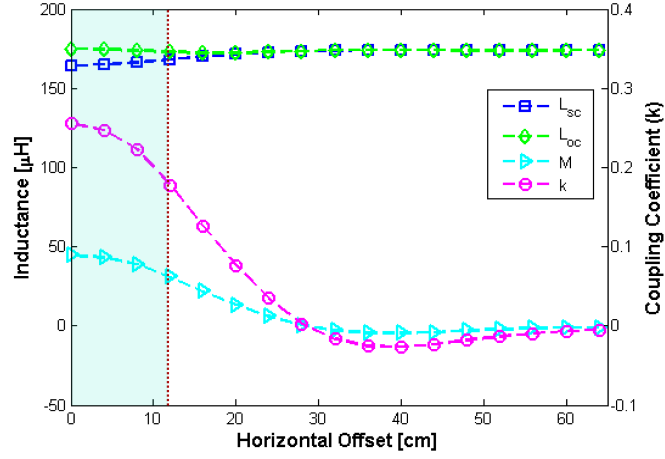


Figure 4.3: Magnetic Characteristics for Power Supply Design

4.1.1 Series Resonant (SLC) Topology

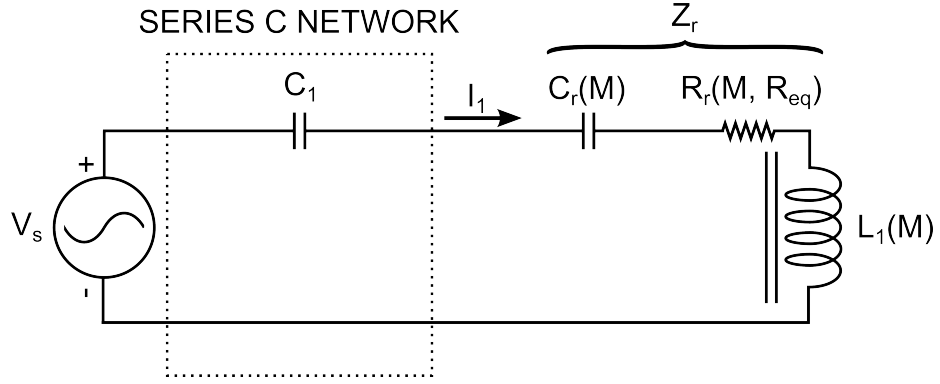


Figure 4.4: Series LC (SLC) Topology

$$C_1 = \frac{L_{2eq}}{\omega_0^2 [L_{\Delta 1} L_{2eq} - M^2]} \quad (4.4)$$

$$L_{\Delta 1} = L_1 - L_{1eq} \quad (4.5)$$

Figure 4.4 shows the simplified equivalent of the SLC power supply. As can be seen, it is essentially made up of a single capacitor in series with the primary coil. As stated previously, the source of HF energy, V_s , is the simplified equivalent of a FB switching network, where the frequency of operation is that of the fundamental component of the square wave output of the conventional FB inverter. The other components in series with the coil are not actual discrete components but, as noted in section 2.3.2, are the virtual components that are reflected through the magnetic coupling from the secondary side and load the primary power supply. The reflected capacitance is a function of M , and the reflected resistance is a function of both M and R_{eq} .

The value of the tuning capacitor C_1 is sized according to equation (4.4) [10] so that when the system is operated at its target frequency, the the resulting equivalent primary inductance, L_{1eq} , seen

by the FB is about 10% of L_1 . This partial series compensation scheme, is equivalent to choosing C_1 so as to fully resonate with L_1 at $f_0 = \frac{1}{2\pi\sqrt{L_1 C_1}}$, and then operating the system at a frequency $f'_0 = 1.05 \times f_0$.

The reason why the SLC power supply is operated slightly (5%) above perfect resonance is that this allows for the reduction of switching power losses in the FB semiconductors by means of the circulating inductive energy associated with the residual inductance L_{1eq} positioning zero voltage across the semiconductors in each leg of the FB just before turn-on. This placement of zero voltage across the switches reduces the instantaneous turn-on power loss that is normally associated with the finite period of time during which the gate-to-source voltage, V_{DS} , of the non-ideal switch is decreasing while its drain current, I_D , is rising. This mode of operation is commonly known as zero-voltage-switching (ZVS), and the specific mechanism used to reduce V_{DS} to zero is the complete discharge of the parasitic drain-to-source capacitance of the switch, C_{DS} , by means of L_{1eq} during the dead-time, t_d , that occurs between the turn-off and turn-on of series switches.

The sizing of C_1 , also takes into account the nominal value of $C_r(M)$ at the system's target operating coupling point; accordingly, C_1 is chosen so that the equivalent capacitance resulting from the combination of $C_r(M_0)$ and C_1 will yield the desired ZVS mode of operation previously described. If the system deviates significantly away from its nominal coupling condition, M_0 , then the resulting variation in the equivalent series tuning capacitance and the non-linear change in L_1 described in section 3.3 will take the FB out of the desired ZVS mode and the power losses will increase dramatically [62]. To prevent the foregoing situation and a potential failure of the semiconductors, the system's switching frequency must be adjusted so as to always maintain ZVS operation. The required frequency control of the SLC topology adds to the complexity of the closed loop controller design.

When C_1 is chosen according to the previously described procedure, the value of the primary current is given as follows:

$$I_1 = \frac{V_S}{\omega L_{1eq}} = \frac{2\sqrt{2}V_{DC}}{\pi\omega L_{1eq}} \sin\left(\frac{\theta_{PS}}{2}\right) \quad (4.6)$$

using this fact along with equation (4.3) the design of the SLC topology can be finalized by determining either the required DC-bus voltage, V_{DC} , or the required HF isolation transformer turns ratio needed to achieve the target I_1 . Selection of V_{DC} assumes that the DC-bus voltage can be controlled at will, such as would be the case if the system had an intermediate buck or boost converter stage between the utility input and the FB. On the other hand, selection of a suitable HF transformer turns ratio assumes that the DC-bus voltage is fixed.

Given the target range of coupling chosen for this work, it was determined that the FB switching frequency would have to be adjusted according to the characteristic shown in Fig.4.5 so as to maintain ZVS. Moreover, the value of C_1 was chosen as $0.2 \mu\text{F}$.

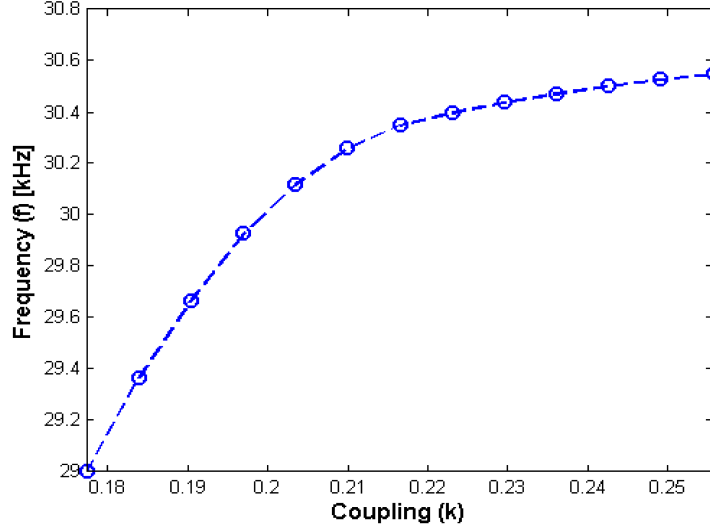


Figure 4.5: SLC FB Switching Frequency for Sustained ZVS Operation

4.1.2 Hybrid Series-Parallel Resonant (LCL) Topology

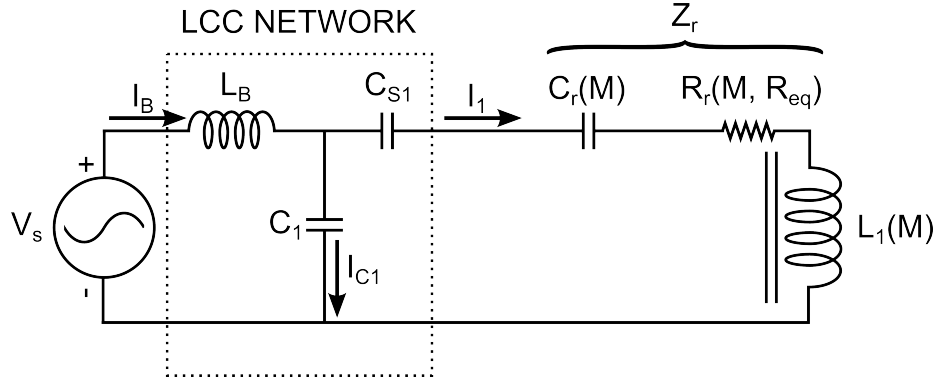


Figure 4.6: Series-Parallel (LCL) Topology

Figure 4.6 shows the simplified circuit equivalent of the LCL power supply. As can be seen, it has two more discrete energy storage elements in its resonant tank, namely the bridge inductance, L_B , and the partial series compensation capacitance, C_{S1} . This topology is sometimes also referred to as an LCL-T topology because of the characteristic T-shape of the ECN. The series capacitance, C_{S1} , is used to reduce L_1 to a smaller equivalent value, L_{1eq} . The parallel capacitance C_1 , is chosen so as to fully resonate with L_{1eq} at the system's operating frequency. The bridge inductance is used to convert the high frequency voltage source characteristic of the FB to an equivalent current source, for this reason this ECN is sometimes spoken of as being an impedance conversion network (ICN) [60, 58].

A very desirable characteristic of the LCL power supply is that, when operated at resonance, it behaves as a constant current source over a very large range of coupling and loading, making its control loop design easier [63]. This is in contrast with the SLC topology, which is quite sensitive to

changes in coupling and thus requires a combination of DC-bus voltage adjustment and frequency modulation to maintain its constant current source operation [1].

Another feature of the LCL architecture that is often praised in the literature is that it reduces the current stress of the bridge semiconductors by constraining the large reactive resonant currents to flow only in the resonant tank [37]. The FB only sources the current associated with the real power flow and the resonant tank losses. The decrease of the bridge current results in a reduced on-time conduction loss for the semiconductors. Because of this, the efficiency of the FB during switching can still be maintained high despite the fact that the switches are not soft-switched as with the SLC topology.

The design equations that govern the sizing of the LCL ECN are as follows:

$$L_{1eq} = \frac{X_1}{\omega_0} \quad (4.7)$$

where X_1 is the effective reactance of the primary coil (after partial series compensation) required to achieve the target value of I_1 :

$$X_1 = \frac{V_S}{I_1} = \frac{2\sqrt{2}V_{DC}}{\pi I_1} \sin\left(\frac{\theta_{PS}}{2}\right) \quad (4.8)$$

The design equation for the partial series compensation capacitance is given as:

$$C_{S1} = \frac{L_{2eq}}{\omega_0^2[L_{\Delta 1}L_{2eq} - M^2]} \quad (4.9)$$

where $L_{\Delta 1}$ is once again given by:

$$L_{\Delta 1} = L_1 - L_{1eq} \quad (4.10)$$

The parallel resonant tuning capacitance C_1 is obtained from:

$$C_1 = \frac{1}{\omega^2 L_{1eq}} \quad (4.11)$$

and the bridge inductance is in practice set to be 10% larger than the value of L_{1eq} , so as to ensure that the inverter will always sees lagging/inductive load:

$$L_B = 1.1 \times L_{1eq} \quad (4.12)$$

The reason why the design is carried out so as to ensure that the switching network always sees a lagging load is that if the bridge were to ever become capacitively loaded, then the semiconductor losses would increase significantly due to large reverse recovery currents in the semiconductor's intrinsic body diode [28].

As was the case with the SLC design strategy, the selection of the capacitance C_{S1} takes into account the reflected virtual capacitance $C_r(M_0)$ [37]. Table 4.2 summarizes the values selected for the power supply using the aforesaid methodology. The bridge inductance, L_B , could be implemented with an actual inductor, but by using cost saving methods described in the next section it can be implemented

by means of the parasitic integrated inductance of the HF isolation transformer.

Table 4.2: LCL Network Values

Component Name	Value
C_{S1}	$0.27 \mu\text{F}$
C_1	$0.60 \mu\text{F}$
L_B	$49.25 \mu\text{H}$

4.1.3 HF Isolation Transformer Design

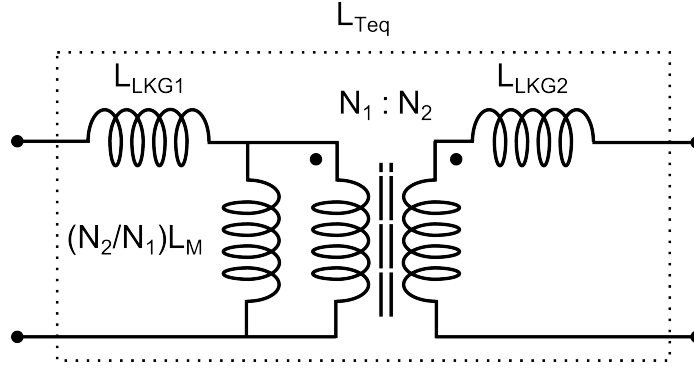


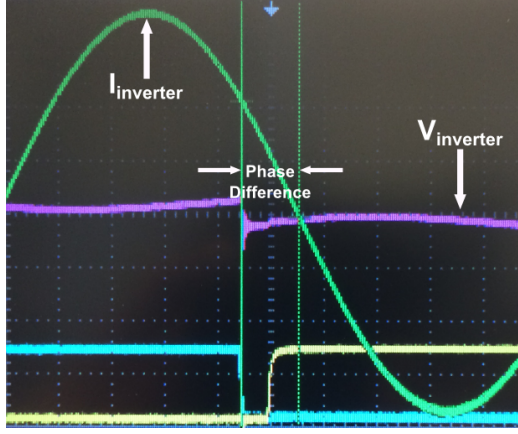
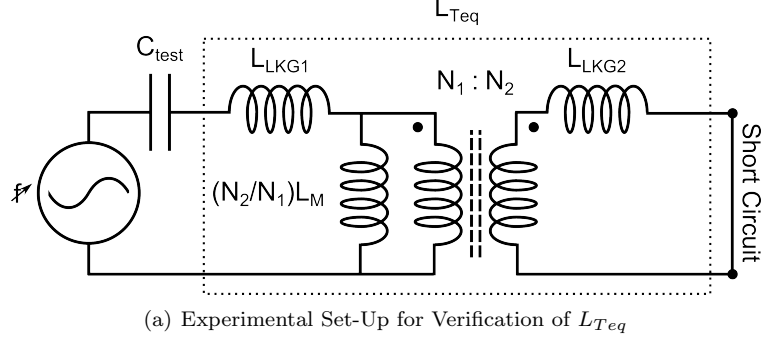
Figure 4.7: HF Isolation Transformer Equivalent Circuit Model

The design of the HF isolation transformer requires the selection of the following:

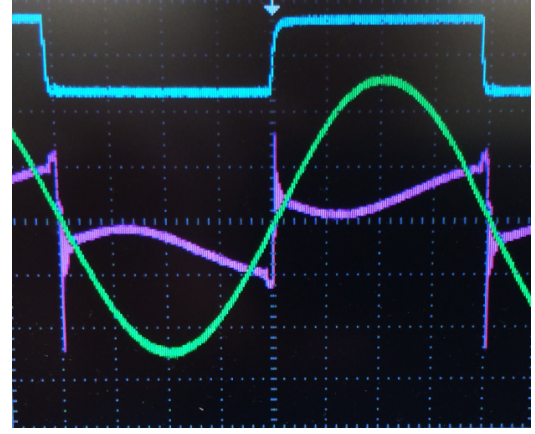
1. Core material with minimum power loss characteristics at the operating frequency.
2. Number of primary and secondary turns; equivalently, transformer's turns ratio.
3. Conductor gauge.
4. Core shape, winding window area, and volume that will house the required number of turns for the chosen conductor gauge and ensure that saturation does not occur at the peak operating flux density.

The design equations and iterative procedure to meet the above listed requirements is very well established in the literature, and a number of sources and application notes were used to carry out the design [64, 65, 66, 67, 68, 69]. The final design used two stacked Ferroxcube 3C94 C-cores. The magnetic circuit of the C-cores was completed with two stacked I-cores having the same with as the C-cores. The shape of the transformer was chosen so that it could be gapped in a controllable manner. The turns ration was approximately 1:1, given that the available DC link input voltage allowed for this choice to be made, thereby making the design and characterization of the windings simpler.

The key issue that is worthy of further consideration is the ability to design the transformer with a controllable and precise amount of leakage inductance. In most applications, the designer's goal is to minimize, parasitic elements as much as possible, but for the design of the LCL power supply, the



(b) L_{Teq} and C_{test} Above Resonance



(c) L_{Teq} and C_{test} At Resonance

Figure 4.8: Experimental Measurement of L_{Teq}

objective is quite the opposite. As stated at the onset of this chapter and in the last section, because the HF isolation transformer is a common element to both power supply topologies, its parasitic attributes can be used as the bridge inductance, L_B , of the LCL ECN, resulting in a reduction in the number of components and cost. For this constructive utilization of the parasitics to be possible, they must be controllable by the designer. Very few references in the literature were found that provide practical direction on how to achieve this particular part of the transformer design. The only available reference found is [38]. In the foregoing reference the authors provide a very rough estimate of the transformer's total equivalent inductance, L_{Teq} , in terms of its magnetizing inductance, L_m , its secondary series leakage inductance, $L_{2lk g}$, and the coupling coefficient. The expression that relates all of the foregoing is:

$$L_{Teq} = (1 - k^2)(L_m + L_{2lk g}) \quad (4.13)$$

With an LCR meter all required quantities in equation (4.13) can be measured. For example, the leakage inductances can be obtained by shorting the the winding that is opposite to the one connected to the LCR terminals. The magnetizing inductance on the other hand, can be obtained by subtracting the primary leakage inductance from the total inductance seen by the LCR meter when the opposite winding is open circuited. Finally, the coupling coefficient can be obtained with

the following relationship:

$$k = \sqrt{1 - \frac{L_{L1lk_g}}{L_m + L_{1lk_g}}} \quad (4.14)$$

Using the above expressions an approximation of the total equivalent inductance, L_{Teq} , presented to the rest of the network was obtained. In order to validate the foregoing estimate, the test scheme illustrated in figure 4.8(a) was used, where a known capacitance, C_{test} , is placed in series with the transformer and then driven with the inverter at the resonant frequency defined by L_{Teq} and C_{test} $\left(f_0 = \frac{1}{2\pi\sqrt{L_{Teq}C_{test}}}\right)$. By observing the phase difference between the inverter's output voltage and current it was then possible to determine whether the system was above or below resonance. Most of the time, the system was slightly above resonance as evidenced by a slightly lagging current (Fig.4.8(b)). At this point the frequency was decreased in small steps until the voltage and current were perfectly in phase, indicating that the system was operating at perfect resonance (Fig.4.8(c)). It is important to note that if the same test is performed with a signal generator instead of the inverter, the results are quite different; this is likely because there isn't enough current to drive the transformer's magnetizing branch inductance. It is also important to note that C_{test} may also be placed in series on the secondary side of the transformer and the same result will be realized.

Having thus obtained the actual resonance frequency and knowing the value of C_{test} , it was then possible to compute the actual equivalent inductance of the transformer with the following relationship:

$$L_{Teq} = \frac{1}{C_{test}(2\pi f_0)^2} \quad (4.15)$$

Using the previously described procedure iteratively, the transformer's equivalent inductance was obtained for different designs. In order to increase L_{Teq} in a controllable manner, the transformer's gap was increased in small steps until it produced a total equivalent inductance of 67.28 μH . This value is larger than the required 49.25 μH , but it was purposefully over-sized so as to have head-room for potential future adjustments that might be needed if the system were to be scaled up or down as part of ongoing research. For the current design, the excess inductance will be trimmed by means of partial series compensation achieved with the DC-blocking capacitor that is placed on the primary side of the transformer. Figure 4.7 shows the core shapes used in the physical implementation. To ensure that the core would not get close to its saturation point in the B-H curve, two C and I cores were stacked together for the final implementation. Table 4.3 summarizes the measured values of all relevant transformer inductances for the final design.

Table 4.3: Measured HF Transformer Attributes

Name	Value
L_{LKG1}	77.6 μH
L_M	278.6 μH
L_{LKG2}	78.7 μH
k	0.85
L_{Teq}	67.28 μH

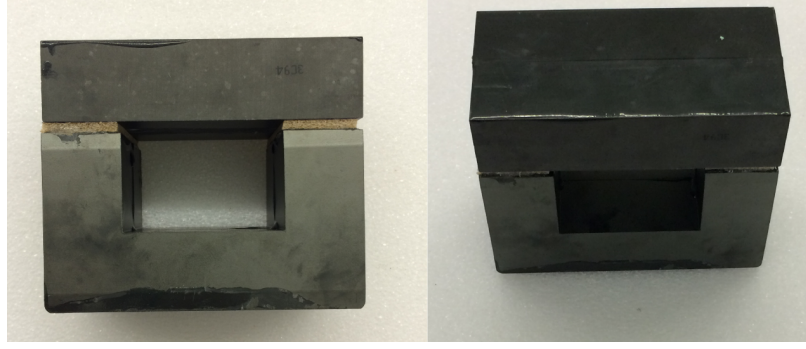


Figure 4.9: Gapped Transformer Core

4.2 Determination of Component Ratings

Table 4.4: LCL and SLC Voltages and Currents

	LCL	SLC
I_B	$\frac{j(\omega^2 L_{1eq} C_1 - 1)}{\omega L_B (1 - \omega^2 L_{1eq} C_1) + \omega L_{1eq}} V_S$	N/A
I_{C1}	$\frac{-\omega^2 L_{1eq} C_1}{\omega L_B (1 - \omega^2 L_{1eq} C_1) + \omega L_{1eq}} V_S$	I_1
I_1	$\frac{1}{j[\omega L_B (1 - \omega^2 L_{1eq} C_1) + \omega L_{1eq}]} V_S$	$\frac{V_S}{j\omega L_{1eq}}$
V_{LB}	$\frac{-\omega L_B (\omega^2 L_{1eq} C_1 - 1)}{\omega L_B (1 - \omega^2 L_{1eq} C_1) + \omega L_{1eq}} V_S$	N/A
V_{C1}	$\frac{j\omega L_{1eq}}{\omega L_B (1 - \omega^2 L_{1eq} C_1) + \omega L_{1eq}} V_S$	$\frac{-V_S}{\omega^2 C_1 L_{1eq}}$
V_{CS1}	$\frac{-1}{C_{S1} \omega^2 [L_B (1 - \omega^2 L_{1eq} C_1) + L_{1eq}]} V_S$	N/A
V_{L1}	$\frac{\omega L_1}{\omega L_B (1 - \omega^2 L_{1eq} C_1) + \omega L_{1eq}} V_S$	$\frac{L_1}{L_{1eq}} V_S$

Once the component values on both the primary and secondary have been obtained, their respective ratings must be determined so as to ensure their safe operation. The equations governing the ratings of the secondary side elements were summarized in section 2.3.2. Similarly, the expressions governing the ratings of the primary side elements are obtained by applying standard circuit analysis techniques to the primary power supply topologies designed in the previous sections (4.4)

As is seen from the complete mathematical model presented thus far, the voltages and currents will vary with changes in coupling and loading. Consequently, the establishment of the peak ratings requires that all of the system's equations be swept over their full range of coupling and loading and that the maximum values of each element's voltage and current be ascertained. This task is made even more challenging because as noted in section 3.3, when the coupling changes, so do the mutual and self inductances of the coupled coils. To be able to tackle the said computationally intensive task, a MATLAB routine was developed that steps through the system's range of coupling and loading, and evaluates each expression in the mathematical model with the respective values of mutual and self inductance at the given coupling point for a fixed load value. In like manner, the routine evaluates all expressions at a fixed coupling point while varying the load over the desired range. The function developed reads all of the measured magnetic data from an excel spreadsheet

and stores it in a three dimensional array. Each column in the array holds a different magnetic attribute, while each page holds a set of measurements of these attributes for different coil-to-coil separation distances. For example, column one holds the axial misalignment distance, column two holds the short circuit self-inductance (L_{sc}), column three holds the open circuit self-inductance (L_{oc}), column four holds the mutual inductance (M), and column five holds the coupling coefficient (k). Each row in the array represents the measurement of the magnetic attributes at a given axial misalignment distance. The resulting voltage and current ratings for the sweeps of coupling and loading are stored in two different result arrays, one for the coupling sweep and another for the loading sweep. Upon completing the sweeps, the routine then compares all of the peak ratings of both result arrays for each circuit element and extracts the maximum values. Much as was the case with I_1 , the max ratings obtained from sweeping the theoretical model serve only as an initial reference value for the design, and may have to be adjusted upon evaluation of the physical system implementation.

The following is a summary of the peak ratings obtained based on the MATLAB routine:

Table 4.5: Nominal Design Specifications

Component Name	LCL Rating	SLC Rating
C_{S1}	20.56A/0.89kV	N/A
C_1	46.23A/0.547.32kV	20.56A/0.778kV
L_1	20.56A/0.878.60kV	20.56A/0.878kV
L_B	44.3A/155.94V	N/A
$S_1 - S_4$	44.3A/230V	20.56A/230V

It is relevant to mention that the previously stated sweeping of the system's coupling cannot be done with SPICE simulators because, despite having parametric sweep capabilities of up to six variables at the time, the sweeping of each variable is done independently of all the others. As previously stated, the design of the IPT system requires that the dependencies of the self-inductances on the coupling be accounted for in the sweep routine. In view of the foregoing, this approach adds novelty to the state of the art.

4.3 Switching Network Gate Driver Design

In order to turn on the power semiconductors in the in the FB, a suitable gate driver must be designed. The role of the gate driver is to take a low power pulse (generally around 3.5 V and below 10 mA) from the controller's logic outputs and reproduce the same pulse shape, but with 15 V amplitude and an initial transient peak current that could range anywhere from 1 to 4 amps, depending on the desired switching speed for the range of frequencies used in wireless EV charging. One of the great challenges in achieving the foregoing goal in a FB topology is that the high-side switches ($S1$ and $S3$ in Fig. 4.1) don't have a fixed source terminal voltage, but rather, they are always floating from the negative DC-bus voltage to the positive one. This floating potential presents a challenge because in order to switch and maintain the semiconductor on, a steady 15 V must be applied between the gate and source terminals of the switch for the entire duration of the on-time.

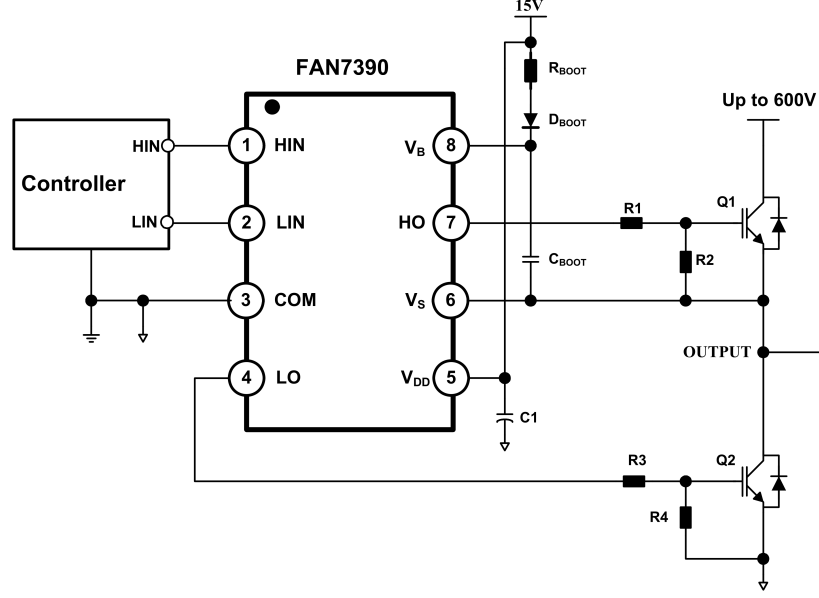


Figure 4.10: Bootstrap Half-Bridge Gate Driver

There are a number of possible schemes available to overcome the floating voltage problem of the high-side switches in the FB inverter [70, 71], but by far the easiest and most economic one is the use of insulated, monolithic, high-voltage, gate-driver ICs. These ICs use the bootstrap capacitor method to place a steady 15 V across the high-side switches gate-to-source terminals. Figure 4.10 shows the schematic of the gate driver IC used to implement the gate driver network of the FB that was implemented in this work. Capacitor C_{BOOT} is charged to 15 V through the forward biased D_{BOOT} during the on-time of the low-side switch Q_2 , so that when Q_2 turns off D_{BOOT} becomes reversed biased and the stored energy across the capacitor's plates remains constant and is positioned to supply the required transient gate-charging current that the high-side switch, Q_1 , will need to achieve full turn-on. The peak transient current, I_G , essentially charges the effective gate-to-source capacitance of the semiconductor until it reaches 15 V.

The selection of the appropriate gate-driver IC requires that the semiconductor's switching characteristics be already in hand. In particular, the switch's characteristic plot of V_{GS} Vs. Q_G must be referenced for the design. In this case, the switch chosen to implement the FB had the characteristic shown in figure 4.11. The procedure followed is to find the required gate charge that the switch would need in order to bring its gate-to-source voltage up to the turn-on voltage level. If the characteristic provided in the datasheet is limited to 10 V, as is the case with many manufacturers, the design will require that the characteristic be extrapolated so as to obtain the required gate-charge at the target voltage level.

Once the needed gate-charge is known, then the required gate-charging current can be readily obtained by means of the following relationship:

$$I_G = \frac{Q_G}{t_{p(on)}} \quad (4.16)$$

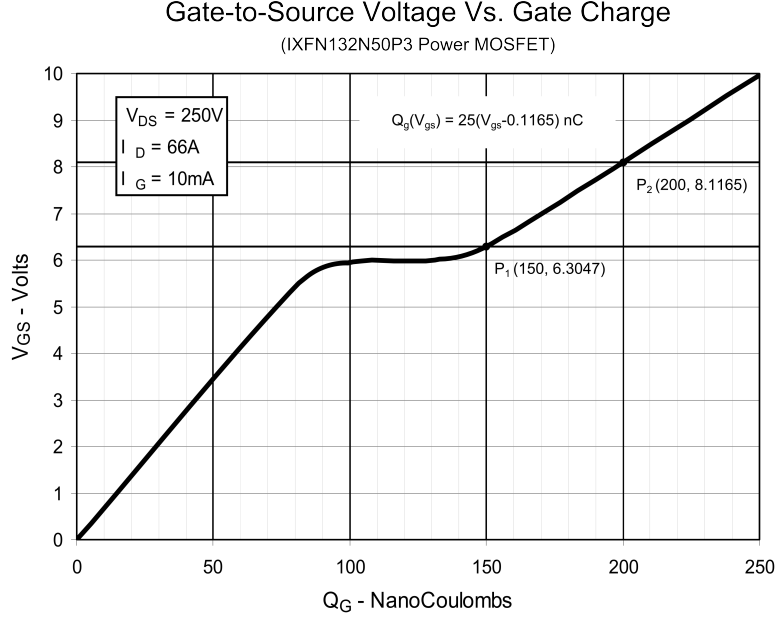


Figure 4.11: Gate-Source Voltage Vs. Gate Charge

where $t_{p(on)}$ is the desired turn-on transition time, and should be selected to be no smaller than the sum of the semiconductor's turn-on delay and rise time. Next the gate driver's required power dissipation capability is calculated with knowledge of the effective gate capacitance, C_G , the switching frequency, f_s , and the gate driver's supply voltage, V_{DD} as follows:

$$P_{GD(min)} = C_G \times V_{DD}^2 \times f_s \quad (4.17)$$

the effective gate capacitance is defined as:

$$C_G = \frac{Q_G}{V_{GS}} \quad (4.18)$$

With I_G and $P_{GD(min)}$ in hand, the search for a suitable gate-driver IC can be completed. For this design, the required I_G was close to 3A, so a gate driver that could source/sink 4A was selected. The FAN7390 is a half bridge gate-driver, so that two ICs must be used in order to drive the two legs of the FB.

Once a gate driver with the suitable current sourcing and sinking capabilities has been selected, the gate resistances, R_G , that will interface it to the power semiconductor and set the target I_G must be sized in terms of their resistance and power rating. The selection of an appropriate R_G value uses the following relationship:

$$R_{G(min)} = \frac{V_{G(on)} - V_{G(off)}}{I_{G(on/off)PEAK}} \quad (4.19)$$

where $V_{G(on)}$ is the on-time gate-to-source voltage, conventionally set to be around 15V, and $V_{G(off)}$ is the off-time gate-to-source voltage, which is simply zero when MOSFETs are used as the power semiconductor.

To estimate the required power rating of R_G , the RMS value of I_G must be obtained. Figure 4.12 shows the gate current waveform during the turn-on and turn-off transitions of the semiconductor (Black trace) as well as the gate-to-source voltage (Blue trace). It is perceivable that they are exponential in nature. To simplify that computation of $I_{G(RMS)}$, the exponential waveforms can be approximated with a narrow right triangle pulse shape, which in turn results in the following compact expression:

$$I_{G(RMS)} = I_{G(on)PEAK} \times \sqrt{\frac{k}{3}} \quad (4.20)$$

where k is defined in terms of the switching frequency, f_{sw} and the turn-on transition time, $t_{p(on)}$, as:

$$k = t_{p(on)} \times f_{sw} \quad (4.21)$$

the required minimum power rating of R_G is thus given as:

$$P_{RG(min)} = I_{G(RMS)}^2 \times R_{G(min)} \quad (4.22)$$

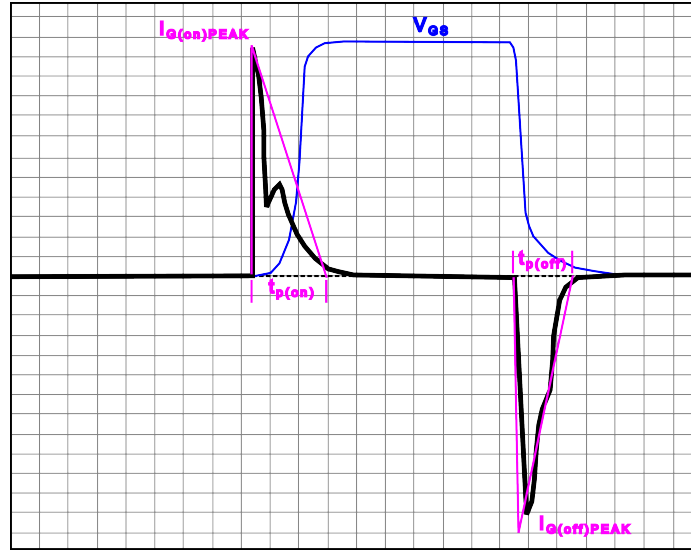


Figure 4.12: Gate Current and Gate-to-Source Voltage Waveforms

The next step is the determination of the capacitance values for C_{BOOT} and C_1 , as well as the determination of the ratings for all of the bootstrap network components.

The value of C_{BOOT} is determined according to the following relationship:

$$C_{BOOT} = \frac{Q_{TOTAL}}{\Delta V_{BOOT}} \quad (4.23)$$

where Q_{TOTAL} is the total amount of charge to be supplied by the capacitor during the turn-on transient and is given as:

$$Q_{TOTAL} = Q_G + (I_{LKCAP} + I_{LKGS} + I_{QBS} + I_{LK} + I_{LKDIODE}) \times t_{on} + Q_{LS} \quad (4.24)$$

the components that sum-up to Q_{TOTAL} in (4.24) are defined as follows:

1. Q_G = Total gate charge obtained from the semiconductor's V_{GS} Vs. Q_G plot.
2. Q_{LS} = Charge required by the IC's internal level shifter (3nC for most HVIC gate drivers).
3. I_{LKGS} = Semiconductor's gate-source leakage current.
4. I_{LKCAP} = Bootstrap capacitor leakage current (zero for ceramic capacitors).
5. I_{QBS} = Bootstrap circuit quiescent current.
6. I_{LK} = Bootstrap circuit leakage current.
7. $I_{LKDIODE}$ = Bootstrap diode leakage current.

t_{on} is the high-side switch on-time. ΔV_{BOOT} is the maximum allowable voltage drop across C_{BOOT} during the on-time, which depends on the minimum allowable gate-to-source voltage, $V_{GS(min)}$, that must be maintained during the on-time; ΔV_{BOOT} is obtained in with knowledge of $V_{GS(min)}$, V_{DD} , and the bootstrap diode forward voltage drop, V_F , as follows:

$$\Delta V_{BOOT} = V_{DD} - V_F - V_{GS(min)} \quad (4.25)$$

All of the above listed component parameters are found in the respective component's datasheet.

The function of C_1 is to support both the low-side side driver and the bootstrap capacitor recharge, consequently, a value at least 10 times the value of C_{BOOT} must be selected:

$$C_1 \geq 10 \times C_{BOOT} \quad (4.26)$$

The bootstrap diode used must have the lowest forward voltage drop possible and be capable of ultrafast recovery. Additionally, since during the off-time of the low-side switch the full DC-bus voltage will be applied to D_{BOOT} its peak voltage blocking capability must be chosen accordingly. Table 4.6 summarizes the values and ratings of the components used in the gate driver board designed for this work. Figure 4.13 shows the top and bottom views of the gate driver board constructed for the physical implementation. The gate drive resistors and the bootstrap network capacitors were sized so as to have a large dynamic switching range that allows for switching frequencies as high as 100 kHz. The large dynamic switching range is desirable because the designed system will be used in further research which may call for changes in the system's operating frequency.

Table 4.6: Gate Driver Network Values and Ratings

Component	Value	Rating
GD IC	N/A	4 Apk, 0.5 W
D_{BOOT}	N/A	4 Apk, 300 V, 75ns
C_{BOOT}	1.5 μF	30 V
C_1	15 μF	30 V
R_G	5 Ω	1 W

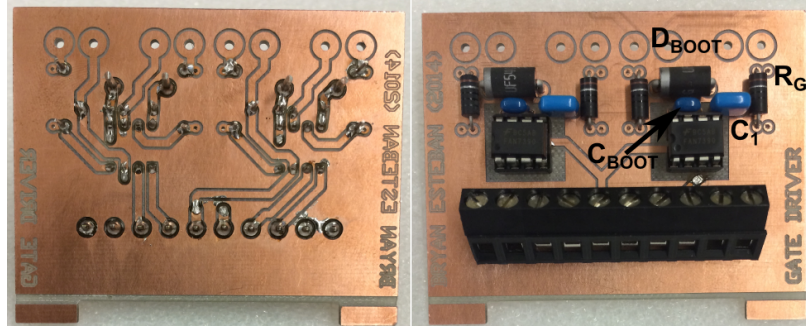


Figure 4.13: Full-Bridge Gate Driver Board

4.4 Physical Implementation

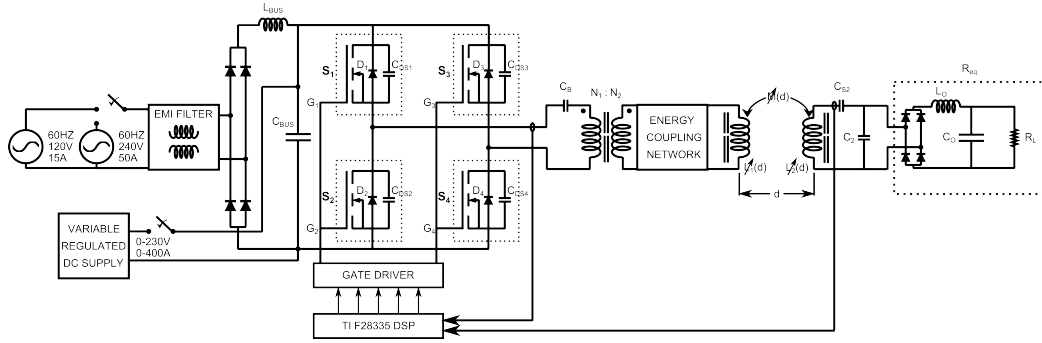


Figure 4.14: Schematic of Completed System Implementation

Figures 4.14 and 4.15 show the complete physical implementation of the designed system. As can be seen from Fig.4.14, the inverter can be energized from three different sources: a standard single phase 120V/15A outlet, a 240V/50A outlet, or with a DC supply. If the system is energized from either of the two AC source ports, then the AC energy is rectified and smoothed by means of an integrated FB line rectifier and LC filter after being passed through an input EMI filter.

Figure 4.14 also shows two integrated current sensors, one in the primary side to sense the primary current, and the other on the secondary side to sense the secondary current. The measurements from these sensors play a key role in the implementation of any control strategy.

To control the gates of the semiconductors in the switching network, a digital signal controller (DSC) was utilized. The DSC was interfaced with a laptop, which served as the main user interface.

Figure 4.16 shows the physical implementation of the two power supply topologies. Figure 4.16(a) is the series resonant architecture, while figure 4.16(b) is the LCL architecture. As might be expected, the overall volumetric footprint of the LCL network is greater than that of the SLC network, making it more complex in terms of the physical manufacturing and assembly process.

Figures 4.14 shows the entire IPT system operating a rated conditions. Finally, figure 4.17 shows oscilloscope captures of the system's waveforms for each power supply topology when operating at rated load.

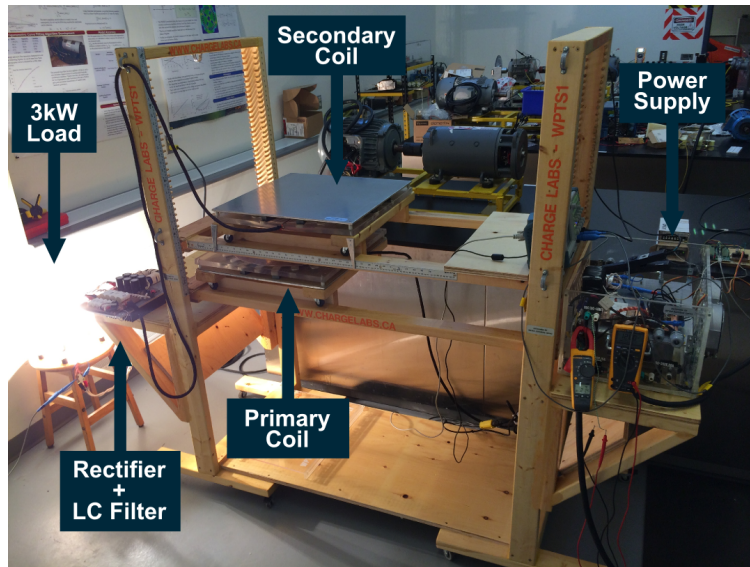
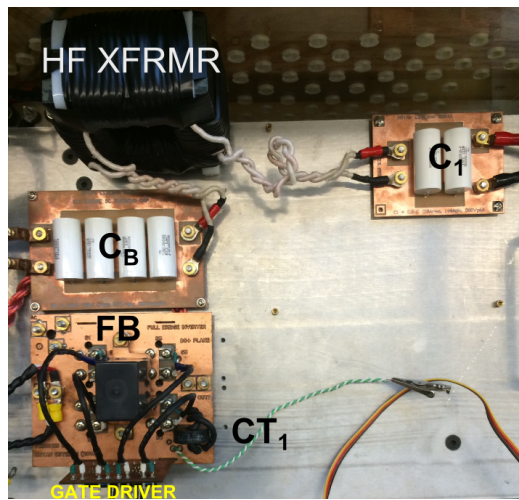
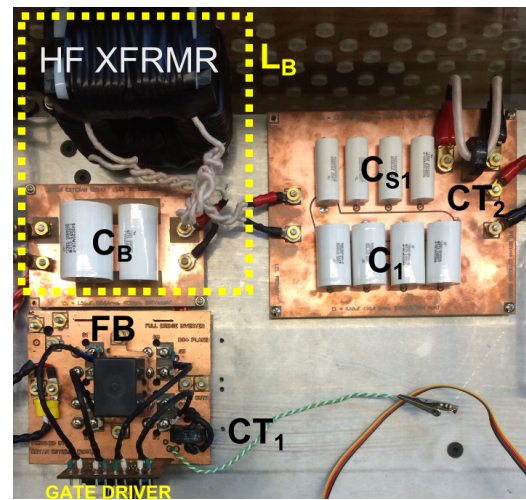


Figure 4.15: Full System Implementation at Rated Power

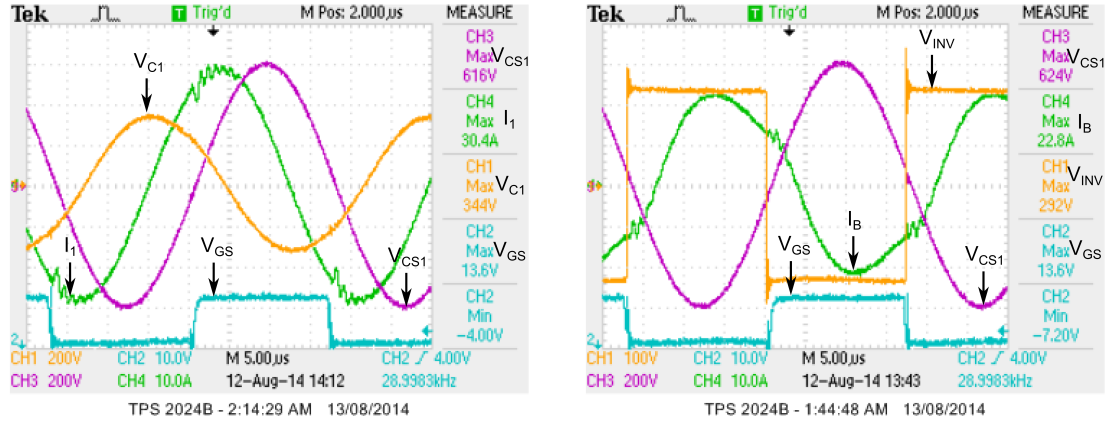


(a) SLC Power Supply

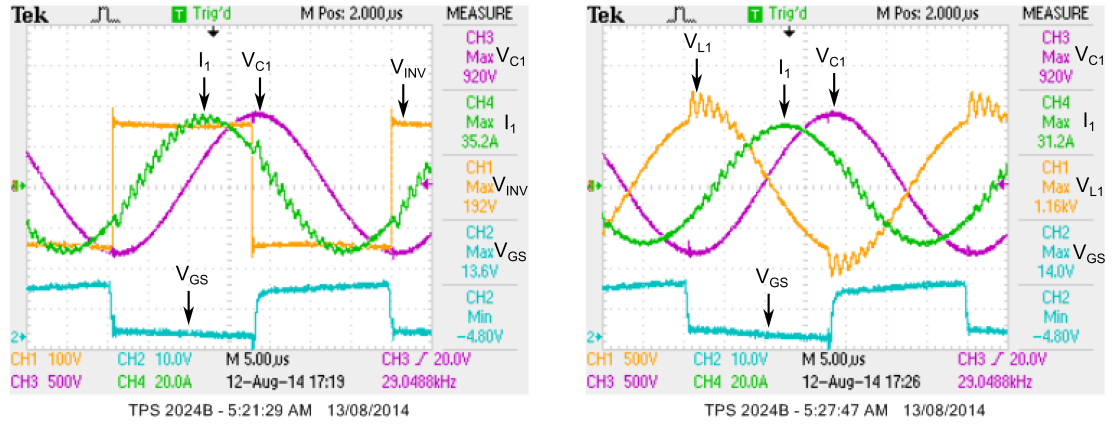


(b) LCL Power Supply

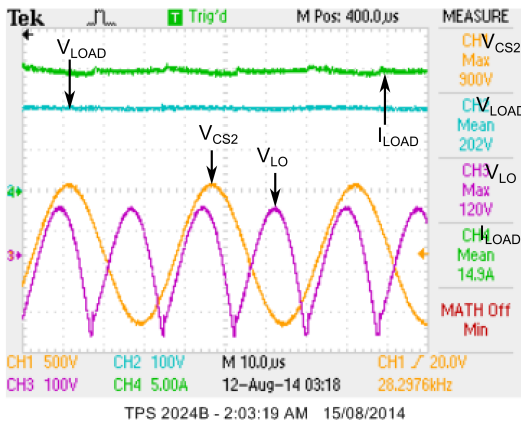
Figure 4.16: Primary Power Supply Implementations



(a) LCL Primary: Yellow= V_{C1} , Green= I_1 , Purple= V_{CS1} , Blue= V_{GS}
 (b) LCL Primary: Yellow= V_i , Green= I_B , Purple= V_{CS1} , Blue= V_{GS}



(c) SLC Primary: Yellow= V_i , Green= I_1 , Purple= V_{C1} , Blue= V_{GS}
 (d) SLC Primary: Yellow= V_{L1} , Green= I_1 , Purple= V_{C1} , Blue= V_{GS}



(e) Secondary Waveforms: Yellow= I_{CS2} , Green= I_L , Purple= V_{Lo} , Blue= V_L

Figure 4.17: System Operating Waveforms at Rated Conditions

Chapter 5

Comparison of Power Supply Topologies

The primary objective of this thesis was to compare the performance of the SLC and LCL power supply topologies in terms of their cost, complexity, efficiency, and power quality. The following sections will present a summary of the comparison's results.

5.1 Complexity and Cost

The SLC topology has the lowest number of discrete energy storage elements, with only one tuning capacitor, C_1 . On the other hand, the LCL architecture requires the use of two more energy storage elements, but by constructively using the parasitic inductance of the common HF isolation transformer the total component count for the LCL power supply is reduced to just two, namely: C_{S1} and C_1 . In view of the higher component count the LCL topology is more complex in its physical implementation and its volumetric space requirements.

On the other hand, when it comes to controllability, the SLC topology is more complex because its switching frequency must be adjusted so as to ensure continued ZVS. This in addition to its primary current's sensitivity to changes in coupling make the overall control of the SLC architecture more challenging.

The cost of a power supply is defined as the ratio of total active power delivered divided by the total VA rating of the of the supply [38]. The VA stored in the tuning components of the power supply is related to its size and associated cost. Hence the ratio of kW/kVA is a good estimate of the kW/\$ of the power supply. In this regard, the cost of the SLC and LCL power supplies when operated at their rated power levels are 0.041 and 0.042 respectively. So as might be expected, the LCL topology has a higher overall cost, though not by much (i.e. 2.41%). Table 5.1 summarizes the stated performance results.

Table 5.1: Summary of Complexity and Cost Performance

Architecture	No. of Capacitors	Cost [W/VA]	Control Complexity
SLC	1	0.041	HIGH
LCL	2	0.042	LOW

5.2 Efficiency

The adoption of wireless over conductive EV charging will require an overall system efficiency that is comparable to the conventional conductive approach. For this to be possible, all system blocks must have the highest efficiency possible. The power supply plays a critical role in the overall efficiency of the IPT system because of its HF switching characteristics

Figure 5.1(a) shows the efficiency of both topologies as a function of the percent of rated loading. As can be seen, the LCL topology is clearly superior over the entire range of loading, achieving a peak efficiency of 96%. The SLC topology on the other hand suffers from poor light load efficiency, dropping to as low as 70%. Furthermore, the peak efficiency of the SLC supply is only 86%. This difference in efficiency is a result of the fact that the bridge power switches of the SLC topology must handle the full resonant current, which increases the semiconductor losses even despite the sustained ZVS operation. On the other hand, the LCL topology is able to maintain very high switching efficiency despite being hard-switched because the bridge stage only handles the current associated with the active power transfer and the resonant tank losses.

Figure 5.1(b) shows the normalized open loop power of each power supply as a function of coupling. The plot shows that as the coupling increases, the power transferred by the SLC power supply actually decreases. This behavior is counterintuitive, but it is readily understood by a close examination of the input impedance of the SLC network. As seen in Fig.5.1(c), as the coupling increases, the reflected impedance seen by the FB of the SLC power supply increases. This increase is primarily because of the real part of the reflected impedance. The result is that the primary current decreases as seen in Fig.5.1(d) and the power transferred is thus lowered. On the other hand, Fig.5.1(b) and Fig.5.1(d) verify the desirable constant current source property of the LCL power supply. Fig.5.1(b) shows that as the coupling increases the power transferred also increases, while Fig.5.1(d) shows that the current remains constant as might be expected.

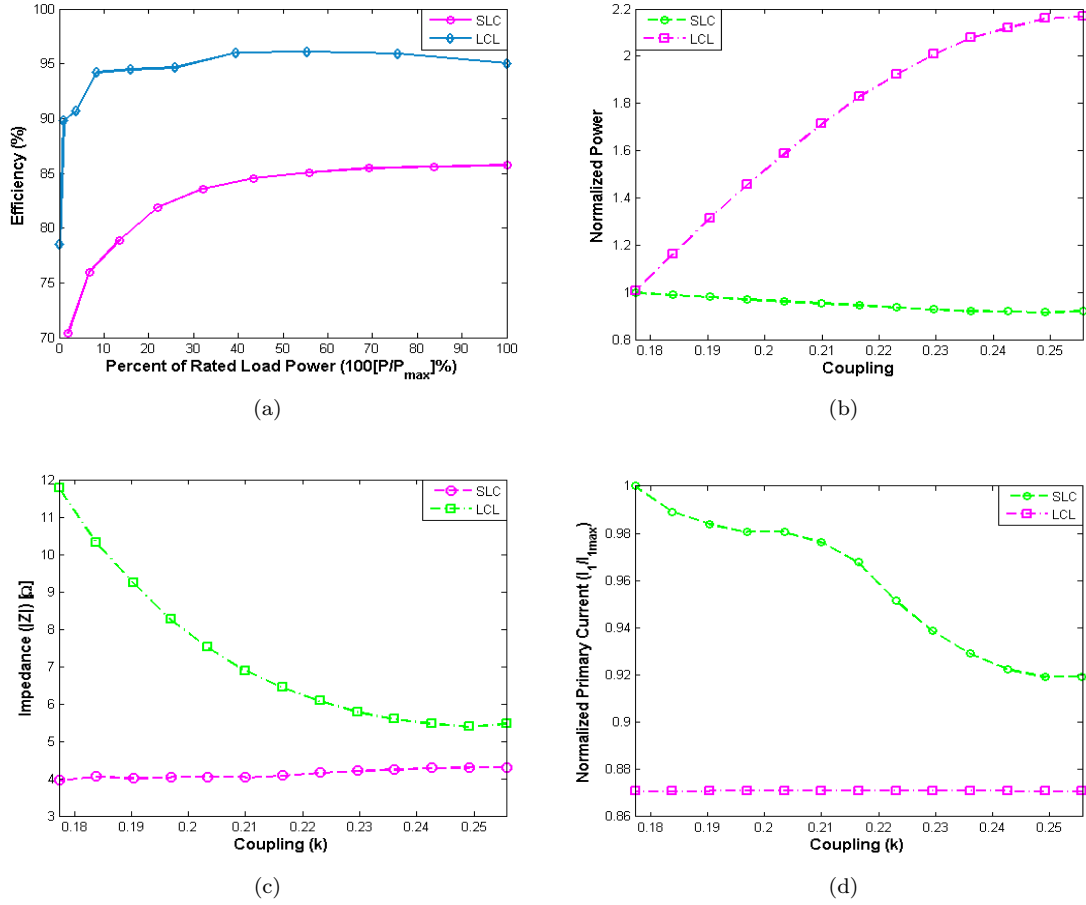


Figure 5.1: Measured Power Supply Attributes

5.3 Power Quality

The precise measurement of a power electronic system's power quality calls for the measurement of total harmonic distortion (THD). Due to BW limitations imposed by the available oscilloscope's power analysis application software, the system's THD could not be measured. For this reason an actual numerical value is not available at this time. Nevertheless, conclusions can still be drawn from the operating waveforms of the two topologies. Referring back to figures 4.17(b) and 4.17(d), it is perceivable from the shape of the waveform that the bridge current, I_B , of the LCL architecture has higher harmonic content than the SLC topology. This is seen in the small notches in the waveform that coincide with the edges of the switching signals.

On the other hand, the current waveform of the SLC topology is perfectly sinusoidal. In view of these observations, it is reasonable to conclude that the SLC topology has lower THD than the LCL topology.

Chapter 6

Conclusion

Table 6.1: Summary of Comparative Study

	No. of Caps.	Cost [W/VA]	Control Complexity	Rated Load Eff.	Light Load Eff.
SLC	1	0.041	HIGH	86%	76%
LCL	2	0.042	LOW	96%	95%

The development of wireless EV charging technologies has gained unparalleled momentum over the later half of the past decade. The release of a formal industry standard governing this novel technology will enable OEM's to bring wireless EVs to market as early as 2016. A key question that remained unanswered until now was: Which of the two power supply architectures commonly used in wireless EV chargers is better in terms of complexity, cost, efficiency and power quality?

This thesis has compared the foregoing two topologies by applying an identical performance test. The results, which are summarized in table 6.1, show that while the SLC topology has slightly lower component count and cost, the LCL topology is superior in terms of its power conversion efficiency over the full range of coupling and loading imposed. Moreover, its constant current source characteristic make its closed loop control implementation easier than the alternative SLC architecture. Because the efficiency of the power supply is a key figure of merit in wireless EV charging, the results presented in this work point to the likely adoption of the LCL topology for a future standardized implementation of wireless EV charging.

Appendix A

Derivations

A.1 Axially Aligned Coils

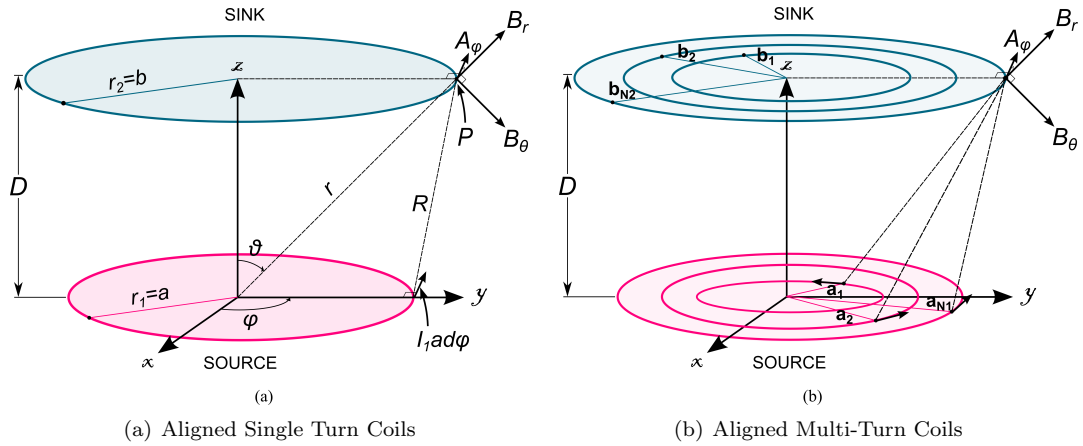


Figure A.1: Analytical Derivation of the Mutual Inductance Using the Magnetic Vector Potential

With reference to Fig. A.1(a), the magnetic vector potential at point P on the secondary is given as:

$$A = \oint \frac{\mu_0 I_1 dl}{4\pi R} \quad (\text{A.1})$$

Where $I_1 dl = I_1 a d\phi$ and I_1 is the rms of the primary current. Using the law of cosines, the distance R is obtained as:

$$R^2 = a^2 + r^2 - 2ar \cos(90 - \theta) \quad (\text{A.2})$$

Taking the square root of both sides of (A.2), converting cos to sin, factoring r^2 , and rearranging terms under the radical in ascending order of powers of r results in:

$$R = r \left(1 - \frac{2a}{r} \sin \theta + \frac{a^2}{r^2} \right)^{1/2} \quad (\text{A.3})$$

For distances r very much greater than the primary radius the third term in the binomial expansion inside the radical approaches zero, this in turn yields:

$$\frac{1}{R} = \frac{1}{r} \left(1 - \frac{2a}{r} \sin \theta\right)^{1/2} \quad (\text{A.4})$$

For a real number σ meeting the criteria $\sigma \ll 1$, the following approximation is well established:

$$\left(1 + \frac{\sigma}{2}\right)^2 = 1 + \sigma + \frac{\sigma^2}{4} \cong 1 + \sigma \quad (\text{A.5})$$

In (A.4) the term $\frac{2a}{r} \sin \theta \ll 1$ by virtue of the fact that $r \gg a$ and $\theta < 90^\circ$. Consequently, letting $\sigma = \frac{2a}{r} \sin \theta$ in (A.4) and rationalizing results in the the following approximation:

$$\frac{1}{\sqrt{1-\sigma}} \times \frac{\sqrt{1+\sigma}}{\sqrt{1+\sigma}} = \frac{\sqrt{1+\sigma}}{\sqrt{1-\sigma^2}} \cong \sqrt{1+\sigma} \cong \sqrt{\left(1 + \frac{\sigma}{2}\right)^2} = \sqrt{\left(1 + \frac{a}{r} \sin \theta\right)^2} = 1 + \frac{a}{r} \sin \theta \quad (\text{A.6})$$

(A.4) may thus be approximated as:

$$\frac{1}{R} = \frac{1}{r} \left(1 + \frac{a}{r} \sin \theta\right) \quad (\text{A.7})$$

Subbing (A.7) for R^{-1} in (A.1) results in:

$$A = \frac{\mu_0 I_1}{4\pi R} \int_0^{2\pi} \left(\frac{1}{r} + \frac{a}{r^2} \sin \theta\right) d\theta \quad (\text{A.8})$$

The r^{-1} term in (A.8) is a monopole term. Since the concept of the magnetic vector potential is founded on the non-existence of magnetic monopoles, the first term may be interpreted as the total vector displacement around the closed loop, and thus becomes zero, leaving only the dipole term, which results in an integral that can be solved in closed form:

$$A = \frac{\mu_0 a^2 I_1 \sin \theta}{2r^2} \quad (\text{A.9})$$

With (A.9) on hand, the mutual flux can now be obtained as the line integral about the secondary loop.

$$\psi_{21} = \frac{\mu_0 a^2 I_1 \sin \theta}{2r^2} \int_0^{2\pi} r \sin \theta d\phi \quad (\text{A.10})$$

$$\psi_{21} = \frac{\mu_0 \pi a^2 I_1 \sin^2(\theta)}{r} \quad (\text{A.11})$$

Dividing (A.11) by I_1 and noting that $r = \sqrt{a^2 + z^2}$ and $\sin \theta = \frac{b}{\sqrt{a^2 + z^2}}$ results in the following expression for the mutual inductance between primary and secondary:

$$M_{21}(z) = \frac{\mu_0 \pi a^2 b^2}{(\sqrt{b^2 + z^2})^3} \quad (\text{A.12})$$

Finally, for a primary with N_1 turns and a secondary with N_2 turns as in Fig. A.1(b), the total mutual flux may be computed by a superposition of the individual flux contributions of each primary turn to each secondary turn, resulting in the following double summation:

$$M_{21}(z, m) = \sum_{i=1}^{N_1} \sum_{j=1}^{N_2} \frac{\mu_0 (\pi a_i^2) (b_j^2)}{(\sqrt{b_j^2 + z^2})} \quad (\text{A.13})$$

A.2 Axially Misaligned Coils

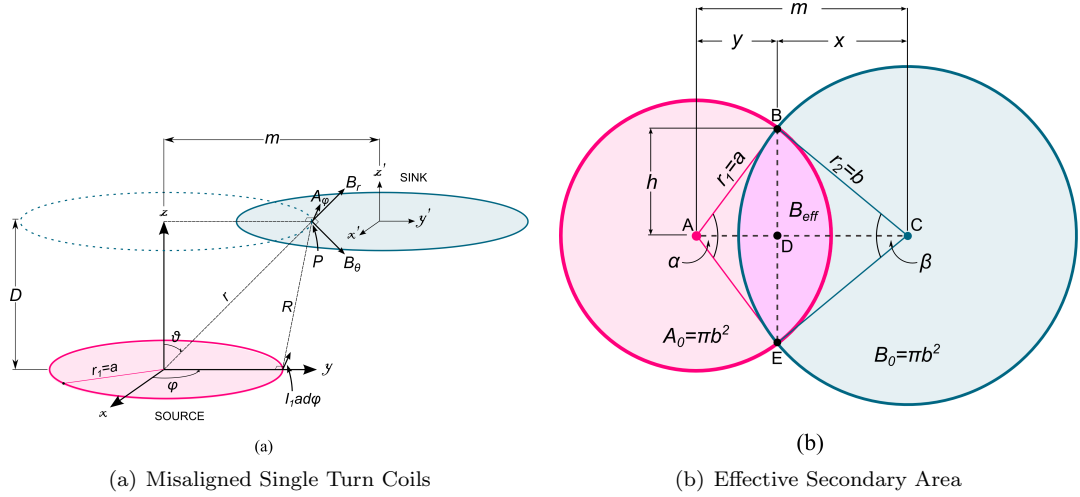


Figure A.2: Analytical Derivation of the Mutual Inductance Using the Magnetic Vector Potential

The modification of (A.13) so as to account for misalignment can be achieved by multiplying the numerator and denominator of (A.12) by π and then rearranging as follows:

$$\psi_{21}(z) = (\pi a^2) (\pi b^2) \frac{\mu_0 I_1}{\pi (\sqrt{b^2 + z^2})^3} \quad (\text{A.14})$$

This latter expression shows explicitly that, in general, the mutual flux is proportional to the area of the secondary as well as the area of the primary. For a misaligned system, it is clear that the only thing that changes from the aligned case is the effective area at the secondary that captures the flux emitted by the primary (i.e. the spatial distribution of the field set up by the primary is unaffected by movements of the secondary).

In view of the foregoing, it is reasonable to conclude that if the effective area that captures the secondary flux can be derived in terms of the misalignment distance m , then it may be replaced in (A.14) so as to yield a general formula that accounts for axial misalignment.

Looking down from the z -axis at the xy -plane in Fig. A.2(a) results in a view like the one shown in Fig. A.2(b). The effective area that captures the primary flux may be interpreted as the intersection of the primary and secondary, B_{eff} . This area is equal to the sum of the areas of the two segments

that result from connecting points B and E. In turn, the area of these segments is simply the area of the sectors they are a part of minus the area of the triangles that each segment is adjacent to (i.e. ΔABE & ΔCBE). To find the foregoing areas, h , y , x , α , and β must be expressed in terms of the target variable m , and the known parameters a and b .

Noting that ΔABD and ΔBCD are similar triangles the following relations may be written:

$$h = \frac{a}{b}x = \frac{b}{a}y \quad (\text{A.15})$$

$$x = \left(\frac{b}{a}\right)^2 y \quad (\text{A.16})$$

$$y = \left(\frac{a}{b}\right)^2 x \quad (\text{A.17})$$

Using $m = x + y$ along with (A.16) and (A.17) the lengths x and y can be expressed as:

$$x = \left(\frac{b^2}{a^2+b^2}\right) m \quad (\text{A.18})$$

$$y = \left(\frac{a^2}{a^2+b^2}\right) m \quad (\text{A.19})$$

The length h can be readily obtained as:

$$h = \sqrt{x^2 + b^2} = \sqrt{y^2 + a^2} \quad (\text{A.20})$$

Finally, the angles α and β are defined as follows:

$$\alpha = 2 \cos^{-1} \left(\frac{y}{a}\right) \quad (\text{A.21})$$

$$\beta = 2 \cos^{-1} \left(\frac{x}{b}\right) \quad (\text{A.22})$$

With all of the needed lengths and angles expressed in terms of m and the two known primary and secondary radii, B_{eff} may be readily shown to be:

$$B_{eff} = \frac{1}{180^\circ} \cos^{-1} \left(\frac{am}{a^2+b^2}\right) \pi a^2 + \frac{1}{180^\circ} \cos^{-1} \left(\frac{bm}{a^2+b^2}\right) \pi b^2 - \left(\frac{m}{a^2+b^2}\right) \left[\sqrt{\frac{m^2}{(a^2+b^2)^2+1}} \right] (a^3 + b^3) \quad (\text{A.23})$$

Equation (A.12) can now be recast as:

$$\psi_{21}(z) = (\pi a^2) (B_{eff}) \frac{\mu_0 I_1}{\pi (\sqrt{b^2+z^2})^3} \quad (\text{A.24})$$

Finally, for the case of a multi-turn primary and secondary, the mutual inductance may once again

be obtained as a summation of individual contributions:

$$M_{21}(z, m) = \sum_{i=1}^{N_1} \sum_{j=1}^{N_2} \frac{\mu_0(\pi a_i^2)(B_{eff,j})}{\pi(\sqrt{b_j^2 + z^2})} \quad (\text{A.25})$$

Bibliography

- [1] G. Covic and J. Boys, “Inductive power transfer,” *Proceedings of the IEEE*, vol. 101, no. 6, pp. 1276–1289, June 2013.
- [2] A. W. Green and J. T. Boys, “10 khz inductively coupled power transfer-concept and control,” in *Power Electronics and Variable-Speed Drives, 1994. Fifth International Conference on*, Oct 1994, pp. 694–699.
- [3] G. A. Covic, G. Elliott, O. Stielau, R. M. Green, and J. T. Boys, “The design of a contactless energy transfer system for a people mover system,” in *Power System Technology, 2000. Proceedings. PowerCon 2000. International Conference on*, vol. 1, 2000, pp. 79–84 vol.1.
- [4] O. Stielau and G. A. Covic, “Design of loosely coupled inductive power transfer systems,” in *Power System Technology, 2000. Proceedings. PowerCon 2000. International Conference on*, vol. 1, 2000, pp. 85–90 vol.1.
- [5] C.-H. Hu, C.-M. Chen, Y.-S. Shiao, T.-J. Chan, and L.-R. Chen, “Development of a universal contactless charger for handheld devices,” in *Industrial Electronics, 2008. ISIE 2008. IEEE International Symposium on*, June 2008, pp. 99–104.
- [6] S. Hui and W. C. Ho, “A new generation of universal contactless battery charging platform for portable consumer electronic equipment,” in *Power Electronics Specialists Conference, 2004. PESC 04. 2004 IEEE 35th Annual*, vol. 1, June 2004, pp. 638–644 Vol.1.
- [7] C.-G. Kim, D.-H. Seo, J.-S. You, J.-H. Park, and B.-H. Cho, “Design of a contactless battery charger for cellular phone,” in *Applied Power Electronics Conference and Exposition, 2000. APEC 2000. Fifteenth Annual IEEE*, vol. 2, 2000, pp. 769–773 vol.2.
- [8] A. Sample, D. Meyer, and J. Smith, “Analysis, experimental results, and range adaptation of magnetically coupled resonators for wireless power transfer,” *Industrial Electronics, IEEE Transactions on*, vol. 58, no. 2, pp. 544–554, Feb 2011.
- [9] All-electric vehicles (evs). [Online]. Available: <http://www.fueleconomy.gov/feg/evtech.shtml>
- [10] J. Huh, W. Lee, G.-H. Cho, B. Lee, and C.-T. Rim, “Characterization of novel inductive power transfer systems for on-line electric vehicles,” in *Applied Power Electronics Conference and Exposition (APEC), 2011 Twenty-Sixth Annual IEEE*, March 2011, pp. 1975–1979.

- [11] H. Wu, A. Gilchrist, K. Sealy, P. Israelsen, and J. Muhs, "A review on inductive charging for electric vehicles," in *Electric Machines Drives Conference (IEMDC), 2011 IEEE International*, May 2011, pp. 143–147.
- [12] Brainstorm green: Ford's alan mulally. [Online]. Available: <http://fortune.com/2012/04/17/brainstorm-green-fords-alan-mulally/>
- [13] N. Kar, K. Iyer, A. Labak, X. Lu, C. Lai, A. Balamurali, B. Esteban, and M. Sid-Ahmed, "Courting and sparking: Wooing consumers? interest in the ev market," *Electrification Magazine, IEEE*, vol. 1, no. 1, pp. 21–31, Sept 2013.
- [14] C. Zell and J. Bolger, "Development of an engineering prototype of a roadway powered electric transit vehicle system: A public/private sector program," in *Vehicular Technology Conference, 1982. 32nd IEEE*, vol. 32, May 1982, pp. 435–438.
- [15] S. Lukic and Z. Pantic, "Cutting the cord: Static and dynamic inductive wireless charging of electric vehicles," *Electrification Magazine, IEEE*, vol. 1, no. 1, pp. 57–64, Sept 2013.
- [16] M. Budhia, G. Covic, and J. Boys, "Design and optimization of circular magnetic structures for lumped inductive power transfer systems," *Power Electronics, IEEE Transactions on*, vol. 26, no. 11, pp. 3096–3108, Nov 2011.
- [17] M. Budhia, J. Boys, G. Covic, and C.-Y. Huang, "Development of a single-sided flux magnetic coupler for electric vehicle ipt charging systems," *Industrial Electronics, IEEE Transactions on*, vol. 60, no. 1, pp. 318–328, Jan 2013.
- [18] A. Zaheer, D. Kacprzak, and G. Covic, "A bipolar receiver pad in a lumped ipt system for electric vehicle charging applications," in *Energy Conversion Congress and Exposition (ECCE), 2012 IEEE*, Sept 2012, pp. 283–290.
- [19] N. Tesla, "System of transmission of electrical energy." Mar. 20 1900, uS Patent 645,576. [Online]. Available: <http://www.google.com/patents/US645576>
- [20] J. T. Boys, G. A. Covic, and A. W. Green, "Stability and control of inductively coupled power transfer systems," *Electric Power Applications, IEE Proceedings -*, vol. 147, no. 1, pp. 37–43, Jan 2000.
- [21] C.-S. Wang, G. Covic, and O. Stielau, "General stability criterions for zero phase angle controlled loosely coupled inductive power transfer systems," in *Industrial Electronics Society, 2001. IECON '01. The 27th Annual Conference of the IEEE*, vol. 2, 2001, pp. 1049–1054 vol.2.
- [22] C.-S. Wang, O. Stielau, and G. Covic, "Load models and their application in the design of loosely coupled inductive power transfer systems," in *Power System Technology, 2000. Proceedings. PowerCon 2000. International Conference on*, vol. 2, 2000, pp. 1053–1058 vol.2.
- [23] J. Boys and G. Covic, "Multi power sourced electric vehicle," Jan. 8 2009, wO Patent App. PCT/NZ2008/000,103. [Online]. Available: <https://www.google.com/patents/WO2008140333A3?cl=en>

- [24] —, “Roadway powered electric vehicle system,” May 5 2011, wO Patent App. PC-T/NZ2010/000,159. [Online]. Available: <https://www.google.com/patents/WO2011016736A3?cl=en>
- [25] J. Boys and A. Green, “Inductive power distribution system,” Mar. 8 1994, uS Patent 5,293,308. [Online]. Available: <http://www.google.com/patents/US5293308>
- [26] M. Budhia, G. Covic, and J. Boys, “Design and optimization of circular magnetic structures for lumped inductive power transfer systems,” *Power Electronics, IEEE Transactions on*, vol. 26, no. 11, pp. 3096–3108, Nov 2011.
- [27] —, “A new ipt magnetic coupler for electric vehicle charging systems,” in *IECON 2010 - 36th Annual Conference on IEEE Industrial Electronics Society*, Nov 2010, pp. 2487–2492.
- [28] G. Elliott, S. Raabe, G. Covic, and J. Boys, “Multiphase pickups for large lateral tolerance contactless power-transfer systems,” *Industrial Electronics, IEEE Transactions on*, vol. 57, no. 5, pp. 1590–1598, May 2010.
- [29] C. Tang, X. Dai, Z. Wang, Y. Sun, and A. Hu, “Frequency bifurcation phenomenon study of a soft switched push-pull contactless power transfer system,” in *Industrial Electronics and Applications (ICIEA), 2011 6th IEEE Conference on*, June 2011, pp. 1981–1986.
- [30] C.-S. Wang, G. Covic, and O. Stielau, “Power transfer capability and bifurcation phenomena of loosely coupled inductive power transfer systems,” *Industrial Electronics, IEEE Transactions on*, vol. 51, no. 1, pp. 148–157, Feb 2004.
- [31] G. Covic, J. Boys, M. Kissin, and H. Lu, “A three-phase inductive power transfer system for roadway-powered vehicles,” *Industrial Electronics, IEEE Transactions on*, vol. 54, no. 6, pp. 3370–3378, Dec 2007.
- [32] “Wireless charging research activities around the world [society news],” *Power Electronics Magazine, IEEE*, vol. 1, no. 2, pp. 30–38, June 2014.
- [33] J. Huh, S. Lee, W. Lee, G. Cho, and C. Rim, “Narrow-width inductive power transfer system for online electrical vehicles,” *Power Electronics, IEEE Transactions on*, vol. 26, no. 12, pp. 3666–3679, Dec 2011.
- [34] S. Choi, J. Huh, W. Lee, and C. Rim, “Asymmetric coil sets for wireless stationary ev chargers with large lateral tolerance by dominant field analysis,” *Power Electronics, IEEE Transactions on*, vol. 29, no. 12, pp. 6406–6420, Dec 2014.
- [35] S. Lee, J. Huh, C. Park, N.-S. Choi, G.-H. Cho, and C.-T. Rim, “On-line electric vehicle using inductive power transfer system,” in *Energy Conversion Congress and Exposition (ECCE), 2010 IEEE*, Sept 2010, pp. 1598–1601.
- [36] W. Lee, J. Huh, S. Choi, X. V. Thai, J. H. Kim, E. Al-Ammar, M. El-Kady, and C. Rim, “Finite-width magnetic mirror models of mono and dual coils for wireless electric vehicles,” *Power Electronics, IEEE Transactions on*, vol. 28, no. 3, pp. 1413–1428, March 2013.

- [37] H. Wu, A. Gilchrist, K. Sealy, and D. Bronson, "A high efficiency 5 kw inductive charger for evs using dual side control," *Industrial Informatics, IEEE Transactions on*, vol. 8, no. 3, pp. 585–595, Aug 2012.
- [38] H. Wu, A. Gilchrist, K. Sealy, P. Israelsen, and J. Muhs, "Design of symmetric voltage cancellation control for lcl converters in inductive power transfer systems," in *Electric Machines Drives Conference (IEMDC), 2011 IEEE International*, May 2011, pp. 866–871.
- [39] J. Miller, C. White, O. Onar, and P. Ryan, "Grid side regulation of wireless power charging of plug-in electric vehicles," in *Energy Conversion Congress and Exposition (ECCE), 2012 IEEE*, Sept 2012, pp. 261–268.
- [40] P. Ning, J. M. Miller, O. C. Onar, C. P. White, and L. D. Marilino, "A compact wireless charging system development," in *Applied Power Electronics Conference and Exposition (APEC), 2013 Twenty-Eighth Annual IEEE*, March 2013, pp. 3045–3050.
- [41] O. Onar, S. Campbell, P. Ning, J. Miller, and Z. Liang, "Fabrication and evaluation of a high performance sic inverter for wireless power transfer applications," in *Wide Bandgap Power Devices and Applications (WiPDA), 2013 IEEE Workshop on*, Oct 2013, pp. 125–130.
- [42] M. Pickelsimer, L. Tolbert, B. Ozpineci, and J. Miller, "Simulation of a wireless power transfer system for electric vehicles with power factor correction," in *Electric Vehicle Conference (IEVC), 2012 IEEE International*, March 2012, pp. 1–6.
- [43] M. Chinthavali, O. Onar, J. Miller, and L. Tang, "Single-phase active boost rectifier with power factor correction for wireless power transfer applications," in *Energy Conversion Congress and Exposition (ECCE), 2013 IEEE*, Sept 2013, pp. 3258–3265.
- [44] O. C. Onar, J. M. Miller, S. L. Campbell, C. Coomer, C. White, and L. E. Seiber, "A novel wireless power transfer for in-motion ev/phev charging," in *Applied Power Electronics Conference and Exposition (APEC), 2013 Twenty-Eighth Annual IEEE*, March 2013, pp. 3073–3080.
- [45] —, "A novel wireless power transfer for in-motion ev/phev charging," in *Applied Power Electronics Conference and Exposition (APEC), 2013 Twenty-Eighth Annual IEEE*, March 2013, pp. 3073–3080.
- [46] A. Karalis, J. D. Joannopoulos, and M. Soljagic, "Efficient wireless non-radiative mid-range energy transfer," *ANNALS OF PHYSICS*, vol. 323, p. 34, 2006. [Online]. Available: <http://www.citebase.org/abstract?id=oai:arXiv.org:physics/0611063>
- [47] A. Kurs, A. Karalis, R. Moffatt, J. D. Joannopoulos, P. Fisher, and M. Soljagic, "Wireless power transfer via strongly coupled magnetic resonances," *Science*, vol. 317, no. 5834, pp. 83–86, July 2007. [Online]. Available: <http://dx.doi.org/10.1126/science.1143254>
- [48] Wicad highly resonant wireless power transfer design software kit. [Online]. Available: <http://witricity.com/products/wicad/>

- [49] Z. Pantic, S. Bai, and S. Lukic, "Zcs lcc -compensated resonant inverter for inductive-power-transfer application," *Industrial Electronics, IEEE Transactions on*, vol. 58, no. 8, pp. 3500–3510, Aug 2011.
- [50] N. Keeling, G. Covic, and J. Boys, "A unity-power-factor ipt pickup for high-power applications," *Industrial Electronics, IEEE Transactions on*, vol. 57, no. 2, pp. 744–751, Feb 2010.
- [51] C.-S. Wang, O. Stielau, and G. Covic, "Design considerations for a contactless electric vehicle battery charger," *Industrial Electronics, IEEE Transactions on*, vol. 52, no. 5, pp. 1308–1314, Oct 2005.
- [52] G. Covic, J. T. Boys, A. M. W. Tam, and J. C. H. Peng, "Self tuning pick-ups for inductive power transfer," in *Power Electronics Specialists Conference, 2008. PESC 2008. IEEE*, June 2008, pp. 3489–3494.
- [53] O. Onar, J. Miller, S. Campbell, C. Coomer, C. White, and L. Seiber, "Oak ridge national laboratory wireless power transfer development for sustainable campus initiative," in *Transportation Electrification Conference and Expo (ITEC), 2013 IEEE*, June 2013, pp. 1–8.
- [54] C.-Y. Huang, J. Boys, G. Covic, and M. Budhia, "Practical considerations for designing ipt system for ev battery charging," in *Vehicle Power and Propulsion Conference, 2009. VPPC '09. IEEE*, Sept 2009, pp. 402–407.
- [55] M. Kissin, J. Boys, and G. Covic, "Interphase mutual inductance in polyphase inductive power transfer systems," *Industrial Electronics, IEEE Transactions on*, vol. 56, no. 7, pp. 2393–2400, July 2009.
- [56] G. Covic and J. Boys, "Modern trends in inductive power transfer for transportation applications," *Emerging and Selected Topics in Power Electronics, IEEE Journal of*, vol. 1, no. 1, pp. 28–41, March 2013.
- [57] H. Wheeler, "Simple inductance formulas for radio coils," *Radio Engineers, Proceedings of the Institute of*, vol. 16, no. 10, pp. 1398–1400, Oct 1928.
- [58] C.-S. Wang, G. Covic, and O. Stielau, "Investigating an lcl load resonant inverter for inductive power transfer applications," *Power Electronics, IEEE Transactions on*, vol. 19, no. 4, pp. 995–1002, July 2004.
- [59] J. Miller, O. Onar, C. White, S. Campbell, C. Coomer, L. Seiber, R. Sepe, and A. Steyerl, "Demonstrating dynamic wireless charging of an electric vehicle: The benefit of electrochemical capacitor smoothing," *Power Electronics Magazine, IEEE*, vol. 1, no. 1, pp. 12–24, March 2014.
- [60] H. Hao, G. Covic, M. Kissin, and J. Boys, "A parallel topology for inductive power transfer power supplies," in *Applied Power Electronics Conference and Exposition (APEC), 2011 Twenty-Sixth Annual IEEE*, March 2011, pp. 2027–2034.
- [61] S. Choi, J. Huh, W. Lee, S. Lee, and C. Rim, "New cross-segmented power supply rails for roadway-powered electric vehicles," *Power Electronics, IEEE Transactions on*, vol. 28, no. 12, pp. 5832–5841, Dec 2013.

- [62] R. Mecke and C. Rathge, "High frequency resonant inverter for contactless energy transmission over large air gap," in *Power Electronics Specialists Conference, 2004. PESC 04. 2004 IEEE 35th Annual*, vol. 3, June 2004, pp. 1737–1743 Vol.3.
- [63] M. Borage, S. Tiwari, and S. Kotaiah, "Analysis and design of an lcl-t resonant converter as a constant-current power supply," *Industrial Electronics, IEEE Transactions on*, vol. 52, no. 6, pp. 1547–1554, Dec 2005.
- [64] W. Hurley, W. Wolffe, and J. Breslin, "Optimized transformer design: inclusive of high-frequency effects," *Power Electronics, IEEE Transactions on*, vol. 13, no. 4, pp. 651–659, Jul 1998.
- [65] H. Karampoorian, P. Gh, A. Vahedi, and A. Zadehgo, "Optimum design of high frequency transformer for compact and light weight switch mode power supplies (smps)," in *GCC Conference (GCC), 2006 IEEE*, March 2006, pp. 1–6.
- [66] M. Kheraluwala, D. Novotny, and D. Divan, "Design considerations for high power high frequency transformers," in *Power Electronics Specialists Conference, 1990. PESC '90 Record., 21st Annual IEEE*, 1990, pp. 734–742.
- [67] T. Filchev, J. Clare, P. Wheeler, and R. Richardson, "Design of high voltage high frequency transformer for pulsed power applications," in *Pulsed Power Conference, 2009 IET European*, Sept 2009, pp. 1–4.
- [68] R. Petkov, "Design issues of the high-power high-frequency transformer," in *Power Electronics and Drive Systems, 1995., Proceedings of 1995 International Conference on*, Feb 1995, pp. 401–410 vol.1.
- [69] J. Liu, L. Sheng, J. Shi, Z. Zhang, and X. He, "Design of high voltage, high power and high frequency transformer in lcc resonant converter," in *Applied Power Electronics Conference and Exposition, 2009. APEC 2009. Twenty-Fourth Annual IEEE*, Feb 2009, pp. 1034–1038.
- [70] *Design Fundamentals of Implementing and Isolated Half-Bridge Gate Driver*, Analog Devices. [Online]. Available: http://www.analog.com/static/imported-files/tech_articles/TA10756-0-5_12.pdf
- [71] A. Pathak and S. Ochi, "Unique mosfet/igbt drivers and their applications in future power electronic systems," in *Power Electronics and Drive Systems, 2003. PEDS 2003. The Fifth International Conference on*, vol. 1, Nov 2003, pp. 85–88 Vol.1.

VITA AUCTORIS

NAME: Bryan Esteban

PLACE OF BIRTH: Manchester, United Kingdom

YEAR OF BIRTH: 1983

EDUCATION: University of Windsor, Windsor, Ontario, Canada
2005-2011 BAsC in Electrical Engineering
University of Windsor, Windsor, Ontario
2012-2014 MASc in Electrical Engineering